

A Search for Mountain Waves in MLS Stratospheric Limb Radiances from the Winter Northern Hemisphere: Data Analysis and Global Mountain Wave Modeling

Jonathan H. Jiang¹, Stephen D. Eckermann², Dong L. Wu¹, and Jun Ma³

¹ Jet Propulsion Laboratory, California Institute of Technology, Pasadena, California, USA

² Middle Atmosphere Dynamics Section, Naval Research Laboratory, Washington, DC., USA

³ Computational Physics, Inc., Springfield, Virginia 22151, USA

Submitted to J.G.R. – Atmospheres.

Short title: Mountain waves in the northern winter stratosphere

Key Words: gravity waves, dynamics, general circulation, global modeling, vortex, jet-stream, and climate

Abstract

Despite evidence from ground-based data that flow over mountains is a dominant source of gravity waves (GWs) for the Northern Hemisphere winter middle atmosphere, GW-related signals in global limb radiances from the Microwave Limb Sounder (MLS) on the Upper Atmosphere Research Satellite (UARS) have shown little direct evidence of mountain waves. We address this issue here by combining a renewed analysis of MLS limb-track and limb-scan radiances with global mountain wave modeling with the Naval Research Laboratory Mountain Wave Forecast Model (MWFM) during MLS measurement days from 1994-1997. MLS variances show characteristics consistent with mountain waves, such as enhanced variance over specific mountain ranges on north/descending (ND) rather than north/ascending (NA) orbits, and annual variations that peak strongly in winter. However, direct comparisons of ND and NA variance maps with MWFM-simulated mountain wave climatologies reveal limited agreement. We develop a detailed “MLS GW visibility function” that accurately specifies the three-dimensional in-orbit sensitivity of the MLS limb-track radiance measurement to a spectrum of GWs with different wavelengths and horizontal propagation directions. On postprocessing MWFM-generated mountain wave fields through these MLS visibility filters, we generate MWFM variance maps for ND and NA orbits that agree substantially better with MLS ND and NA radiance variances, respectively. This combined data analysis and MLS-filtered MWFM modeling leads us to conclude that, in fact, MLS radiances contain a great deal of information on stratospheric mountain wave in the winter Northern Hemisphere at middle and high latitudes. Indeed, many ND and NA variance enhancements can be associated with mountain waves forced by flow over specific mountainous terrain. These include mountain ranges in Europe (e.g.,

Scandinavia; Alps; Scotland; Ural, Putoran, Altai, Hangay and Sayan Mountains; Yablonovyy, Stanovoy, Khingan, Verkhoyansk and Central Ranges), North America (e.g., Brooks Range, MacKenzie Mountains, Queen Elizabeth Islands, Colorado Rockies), southeastern Greenland and Iceland. Our results show that, given careful consideration of the in-orbit sensitivity of the instrument to GWs, middle atmospheric limb radiances measured from UARS MLS, as well as from the new MLS instrument on the Earth Observing System (EOS) satellite, can provide important global information on mountain waves in the extratropical Northern Hemisphere stratosphere and mesosphere.

1. Introduction

Atmospheric gravity waves (GWs) play crucial roles in driving the general circulation and thermal structure of the atmosphere. Quasi-continuous GW breaking at a range of heights around the globe maintains body forces and turbulent diffusion that drive winds, temperatures and chemical constituent distributions well away from those of an atmosphere lacking these processes [e.g., *Andrews*, 1987; *Holton and Alexander*, 2000; *McIntyre*, 2001; *Fritts and Alexander*, 2003]. Indeed, since the spectrum of breaking gravity waves is not resolved in global climate and weather prediction models at present, these unresolved GW processes must be comprehensively parameterized so that models can reproduce realistic circulations on both short and long time scales [see, e.g., *Hamilton*, 1996; *McLandress*, 1998; *Kim et al.*, 2003]. Gravity waves can produce other important effects, such as wave clouds at various heights that can have important follow-on effects on processes such as precipitation and ozone [e.g., *Jensen and Toon*, 1994; *Carslaw et al.*, 1998; *Koch and Siedlarz*, 1999; *Thayer et al.*, 2003]. This has led to a new class of parameterizations of subgridscale gravity wave effects on clouds for global models [e.g., *Cusack et al.*, 1999; *Bacmeister et al.*, 1999].

GWs are generated by a variety of processes in the lower atmosphere [*Fritts and Alexander*, 2003]. Of these, flow over mountains is believed to be one of the dominant sources of GWs, particularly in the extratropics during winter [e.g., *Nastrom and Fritts*, 1992]. The drag produced by the breaking of these so-called mountain waves is important for both short-term weather prediction and long-term climate modeling, and so considerable effort has been devoted to mountain wave drag parameterization schemes for global models [see, e.g., *Kim et al.*, 2003].

Unfortunately, many aspects of GW parameterizations are uncertain and highly simplified, due mainly to a lack of detailed global data on GWs which could be used to intercompare, assess and constrain the various models of these processes currently in use. This paucity of global data has arisen because, until recently, limb and nadir viewing remote-sensing instruments on satellites lacked the spatial or temporal resolution to resolve atmospheric GW perturbations. During the last decade, however, some high-resolution satellite instruments have attained the necessary resolutions and accuracies to provide our first tentative global glimpses of the largest wavelength portions of the GW spectrum.

One of the most important instruments in this critical emerging database has been the Microwave Limb Sounder (MLS) on the Upper Atmosphere Research Satellite (UARS) [Waters *et al.*, 1999]. Since the mid-1990's, UARS MLS 63 GHz radiance fluctuations have been used to study global GW morphologies in the stratosphere and mesosphere [Wu and Waters, 1996a,b; Wu and Waters, 1997; Alexander, 1998; McLandress *et al.*, 2000; Wu, 2001; Jiang and Wu, 2001; Wu and Jiang, 2002; Jiang *et al.*, 2002; Jiang *et al.*, 2003a,b]. When MLS radiances become saturated at the bottom of each scan, they measure air temperature in the saturation layer, and fluctuations of the saturated radiances can be interpreted as temperature perturbations within that layer, after removal of instrument noise [Wu and Waters, 1997].

Previous global maps of MLS radiance variances in the stratosphere and mesosphere showed good correlations between enhanced variance and strong background wind speeds [e.g. Wu and Waters, 1996a,b; Wu and Waters, 1997; McLandress *et al.*, 2000; Jiang and Wu, 2001]. Alexander [1998] showed that much of this structure could be reproduced by a simple source-independent GW ray-tracing model, which accounted for

the Doppler-shifting effects of background winds on the gravity wave spectrum and the finite vertical width of the MLS channel weighting functions, which allowed only those waves with long vertical wavelengths to be resolved. *McLandress et al.* [2000] performed a detailed follow-up study of MLS variances measured by channels 3 and 13 (altitudes $z \sim 38$ km) and used a similar global GW ray model to simulate the observed variance distributions. Their work showed that refraction and observational filtering of waves by background winds alone could not explain all of the structure in MLS GW variance maps. For example, model sensitivity experiments suggested that large increases in stratospheric variances in the summer subtropics and in winter over the southern Andes were superficially consistent with intense local generation of gravity waves from underlying convective and topographic sources, respectively.

Eckermann and Preusse [1999] analyzed a week's worth of infrared limb temperature data acquired by the CRISTA instrument on the Shuttle Pallet Satellite in November, 1994. After isolating stratospheric temperature perturbations, they used simple theory and output from the Naval Research Laboratory (NRL) Mountain Wave Forecast Model (MWFM) to show that enhanced stratospheric temperature fluctuations over the southern tip of South America were produced by mountain waves forced by flow across the Andes. A detailed followup study by *Preusse et al.* [2002] confirmed this using retrieval modeling, GW theory, a mesoscale model and ray-tracing experiments. Given these indications, *Jiang et al.* [2002] conducted a thorough study of stratospheric radiance variances over the southern Andes region, utilizing slightly more than 2 years of MLS limb track data between late 1994 and early 1997. Variances over the Andes exhibited a strong annual variation, peaking in winter, with somewhat weaker wintertime activity in 1996 compared to 1995. These features were reproduced quite well by a detailed MWFM

“hindcast” simulation formulated for this particular time period. *Wu and Jiang* [2002] also reported enhancements of MLS variances over Antarctica that may also be mountain wave-related.

Mountain waves are believed to be more energetic and geographically prevalent in the Northern Hemisphere [*Bacmeister*, 1993; *Fritts and Alexander*, 2003], due to the more extended mountainous landmasses in this hemisphere. Yet little if any progress has been made to date in extracting unambiguous data on mountain waves from MLS radiances in the Northern Hemisphere. *McLandress et al.* [2000] documented highly structured variance distributions in the northern extratropics, but they were unable to draw conclusions as to the sources of this wave activity because strong longitudinal and day-to-day variations in stratospheric wind fields complicated their model-data comparisons. *Jiang and Wu* [2001] further demonstrated how strong variable stratospheric flow fields in the north substantially modulated MLS variances, seemingly masking any signatures of wave sources. Such difficulties do not appear to be unique to MLS. Despite showing clear evidence of enhanced stratospheric temperature variance from gravity waves over deep tropical convection, GPS/MET occultation data have to date yielded little clear evidence of enhanced temperature variances over mountains in the Northern Hemisphere during winter [*Tsuda et al.*, 2000].

Despite these complications, MLS satellite data do show occasional hints of variance enhancements over topography during northern winter. For example, Figure 5b of *McLandress et al.* [2000] shows enhancements in limb track variances over mountainous regions such as Scandinavia, central Eurasia, Ellesmere Island and southern Greenland, where long wavelength stratospheric mountain waves have sometimes been observed [e.g., *Leutbecher and Volkert*, 2000; *Dörnbrack et al.*, 2002]. Furthermore, *Eckermann*

and Preusse [1999] found enhanced CRISTA temperature perturbations over central Eurasia and used MWFM hindcasts to show that they were consistent with energetic stratospheric mountain waves emanating from significant underlying mountain ranges in this region.

Why are mountain waves evident in some satellite observations, yet seemingly absent or obscured in others? Do MLS radiances contain any information on stratospheric mountain waves in the Northern Hemisphere? If not, why not, particularly when clear mountain wave signals appear in MLS data from the Southern Hemisphere [*Jiang et al.*, 2002]? If there is mountain wave information buried within these data, can we extract it to provide much-needed global information on these waves? Motivated by these questions, this paper combines a careful analysis of MLS stratospheric radiance data from the Northern Hemisphere with detailed companion modeling of anticipated global distributions of mountain waves that MLS might resolve. Our scientific approach is as follows: 1) construct improved climatological maps of GW-related MLS variances in the Northern Hemisphere; 2) identify specific zones of variance enhancement that are the likeliest candidates for a mountain wave explanation; 3) analyze variances over these “focus regions” using all available MLS data in ways that test the mountain wave hypothesis further; 4) conduct detailed “hindcast” modeling of these observations using the NRL MWFM, paying particular attention to the instrumental and environmental effects that influence how mountain waves manifest in MLS radiances.

In section 2, we describe the MLS GW variance calculation techniques and their recent improvements. In section 3, we analyze MLS radiance variances in Northern Hemispheric winter and identify geographical regions with potential mountain wave-induced variance enhancements. In section 4, we outline our modeling strategy, which

uses the MWFM to simulate MWs that manifest in MLS radiances. In particular, we develop a complete 3D MLS visibility function which mimics the MLS GW observation, specifically its sensitivity to waves of different wavelengths and horizontal orientations with respect to the MLS LOS. Section 5 compares modeled MWFM fields with the MLS variance data. Results are briefly summarized and discussed in section 6.

2. Computation of MLS Radiance Variances

To derive GW variances from MLS saturated radiances, *Wu and Waters* [1996b] used a straightforward analysis method consisting of three main parts. Our current version of that basic analysis method is outlined below.

2.1 Variance Estimate

For each MLS 63GHz frequency channel, the estimated radiance variance $\tilde{\sigma}^2$ is obtained from n individual measurements of saturated radiances at the bottom of each limb scan, as follows

$$\tilde{\sigma}^2 = \frac{1}{n-2} \sum_{i=1}^n (y_i - a - bz_i)^2 \quad (1)$$

where y_i and z_i are individual radiance and tangent height measurements, respectively, and n is the number of consecutive measurements of saturated radiances along the limb track which are used to form a variance. *Wu and Waters* [1996b] used $n=6$ and we compute these same “six point” variances in this study. The factor $n-2$ in the denominator of (1) comes from reduced degrees of freedom in this variance estimate [*Wu and Waters*, 1997], since a and b are two constraint parameters for y_i and z_i . Because the saturated radiances may depend slightly on tangent height as the limb path length decreases, a

linear trend (described by parameters a and b) is fitted to the radiances to remove both the mean radiance trend and any tangent height dependence.

2.2 Variance Averaging

The next step in the analysis involves substantial averaging of many individual variance estimates $\tilde{\sigma}_j^2$:

$$\tilde{\sigma}^2 = p^{-1} \sum_{j=1}^p \tilde{\sigma}_j^2 \quad (1b)$$

Since these small-scale atmospheric (wave-induced) radiance variances are often transient and weak compared to instrument noise [e.g., *McLandress et al.*, 2000; *Wu*, 2001], the statistical uncertainties in the estimated variances must be reduced via substantial averaging as in (1b) ($p \gg 1$). To a good approximation, the statistical uncertainty (random error) of one given MLS radiance variance estimate $\tilde{\sigma}^2$ can be expressed as [*Wu and Waters*, 1997]

$$|\tilde{\sigma}^2 - \sigma^2| \approx \sqrt{2} \sigma^2 \quad (2)$$

where σ^2 is the true variance. This measurement uncertainty on the right-hand side of (2) is reduced by a factor of \sqrt{p} when p independent variance estimates are averaged as in (1b) [*Wu and Waters*, 1997]. Such averaging is achieved at the expense of the final spatial and temporal resolution of the variance maps, and thus some tradeoff between signal averaging and final resolution must be made. In practice, improvements from the averaging are also ultimately limited by other factors such as atmospheric/noise variance ratio, spatial/temporal resolution, and MLS sampling rate. The statistical uncertainty in the mean variance, discussed here, should not be confused with the large standard

deviations of the MLS variances that can arise due to geophysical variations in the intensity of the local wave fields (see, e.g., Figure 7 of *McLandress et al.*, 2000).

2.3 Noise Estimation and Removal

The final step in the process involves estimating and removing instrument noise variances. The variance in (1) has two main components: instrument noise and atmospheric variance, i.e., $\tilde{\sigma}^2 = \tilde{\sigma}_N^2 + \tilde{\sigma}_A^2$ (here we neglect an additional nonlinear pressure error variance $\tilde{\sigma}_{NL}^2$ that arises only for data from channels 1/15 and 2/14 [*Wu and Waters*, 1997]). We associate the atmospheric component ($\tilde{\sigma}_A^2$) with radiance fluctuations produced by gravity waves and refer to it hereafter as the GW variance. For UARS MLS, the instrument noise $\tilde{\sigma}_N^2$ is frequency (channel) dependent but stable during the entire mission [*Lau et al.*, 1996]. Thus, one way to estimate the instrument noise is to average radiance variances at latitudes (usually near the tropics) where there is little resolved GW activity ($\tilde{\sigma}_A^2 \approx 0$), so that $\tilde{\sigma}^2 \approx \tilde{\sigma}_N^2$. In practice, we estimate the instrument noise from the minimum variance of monthly zonal-mean averages (evaluated globally within equispaced 5° latitude bins). The minimum variances from about 36 months of such averages are themselves then averaged together to yield a mean estimate of the noise variance $\tilde{\sigma}_N^2$ for each MLS channel. These noise variances are within 20% (see Table 1) of the calibrated values [*Wu and Waters*, 1997]. GW variances then follow by subtracting the noise variance: $\tilde{\sigma}_A^2 = \tilde{\sigma}^2 - \tilde{\sigma}_N^2$.

The $\tilde{\sigma}_A^2$ variances originate primarily from GW temperature perturbations resolved by MLS within the saturation layer. Thus $\tilde{\sigma}_A^2$ estimates are available at the 8 MLS channel saturation altitudes ($\sim 28, 33, 38, 43, 48, 53, 61$, and 80 km). Only a small portion of the

atmospheric GW field is resolved by these MLS limb measurements, an effect that must be carefully considered when using $\tilde{\sigma}_A^2$ data to infer information on fundamental gravity wave properties [Alexander, 1998; McLandress *et al.*, 2000]. This “observational filtering” is particularly acute for the six-point variances we consider here (see, e.g., Figure 1 of McLandress *et al.*, 2000]. We provide a thorough discussion of these issues in later sections.

2.4 Further Improvements

In this study we improved the $\tilde{\sigma}_A^2$ calculations in several ways. Specifically, we improved the quality of the channel 1 radiance variances (which saturate at the lowest altitude), the signal-to-noise ratios (SNR) of all the channel variances, and increased the data volume that goes into the mean variance statistics.

We found that the tangent height z_t must be below ~ 14 km in order for channel 1 radiances to satisfy the saturation condition. This cutoff limits the number of individual radiance values for the variance calculations in (1) during normal limb-scan operation to $n \leq 4$. Thus, 4-point limb-scan variances replace the previous 6-point limb-scan variances used in Wu and Waters [1996b] and give more reliable results at lower altitudes. For limb-track data, we still compute 6-point variances but confine ourselves to data with tangent heights $z_t < 14$ km.

To improve the SNR of $\tilde{\sigma}_A^2$, we combined radiances from a pair of channels that are symmetric about the line center before performing the detrending operation in (1). Since the symmetric channels have similar temperature weighting functions and mean noise levels [Wu and Waters, 1997], the variance of the combined channel radiances yields a noise variance about half that from the single channel radiances alone, namely,

$\tilde{\sigma}_{combined}^2 = \tilde{\sigma}_A^2 + \frac{\tilde{\sigma}_N^2}{2}$. This represents a factor of 2 improvement in the variance SNR. It is important to combine the radiances before averaging, otherwise the averaged variances from the two paired channels would only improve the SNR by a factor of $\sqrt{2}$ instead of 2.

[Insert Table 1 here]

Another improvement in the GW variance analysis is to make a full use of all saturated radiances. Instead of cutting off the limb radiances at the same tangent height for all the channels, we make the cutoff height channel-dependent. Because radiances from different channels saturate at different heights, higher cutoff heights increase the number of samples p in (1b), reducing statistical uncertainties.

Finally, the new GW variance data have more accurate geographical registration of the atmospheric volume measured by each channel. Because saturated MLS radiances measure the atmospheric volume on the near side of the tangent point (see, e.g., Figure 2 of *Jiang et al.*, 2003a), the geographical location of this atmospheric volume is displaced from the tangent point, in contrast to the atmospheric volume of unsaturated limb radiances. This correction was not considered in previous MLS GW variance calculations. We found by studying mountain waves and comparing them to model predictions in this work that inferred distributions of wave activity prove particularly sensitive to any such geolocation errors in $\tilde{\sigma}_A^2$.

3. Enhanced MLS Variances Over Mountains

To investigate possible variance enhancements over Northern Hemisphere topography, we focus initially on the limb-track data, which have higher resolution and are more easily analyzed for their GW content than limb-scan data [*McLandress et al.*,

2000]. Figure 1a plots an hemispheric map of mean 6-point limb track radiance variances from channels 3 and 13 (altitude ~ 38 km) during northern winter (December-February) for the years 1994-1997, as acquired during north looking (N) yaw cycles and descending (D) orbit segments. We refer to these hereafter as “ND variances,” $(\tilde{\sigma}_A^2)_{ND}$. NA variances $(\tilde{\sigma}_A^2)_{NA}$ derived from north looking (N) ascending (A) orbits are plotted in Figure 1c. Figure 1b plots a high-resolution map of the topographic elevations of landmasses in the Northern Hemisphere, with major features relevant to potential mountain wave forcing highlighted. This includes major continental mountain ranges, mountainous islands, and the Greenland mountain-ice complex. The major focus is topography poleward of 30°N , since MLS variances equatorward of 30° in Figures 1a and 1c show no significant variance enhancements.

[Insert Figure 1 here]

3.1 Sensitivity of Variances to MLS View Direction

MLS can view low-latitude regions of the atmosphere in any one of four different viewing geometries, which vary with the north-south yaw cycle of UARS and whether the spacecraft is on the ascending (south to north) or descending (north to south) portion of its orbital track. Only north-viewing yaw cycles yield near-hemispheric coverage of the Northern Hemisphere, which limits us to the two ND and NA views introduced in Figures 1a and 1c, respectively. ND and NA variances differ significantly. Most obvious is an overall decrease in intensity and a much “spottier” global distribution of $(\tilde{\sigma}_A^2)_{NA}$ compared to $(\tilde{\sigma}_A^2)_{ND}$. Jiang *et al.* [2003a] found a similar result on plotting ND and NA variance maps over the southern Andes and western USA. The visual correlations with

topography (Figure 1b) are much more striking for $(\tilde{\sigma}_A^2)_{ND}$ in Figure 1a than for $(\tilde{\sigma}_A^2)_{NA}$ in Figure 1c.

This sensitivity to view direction was studied and quantified somewhat by *McLandress et al.* [2000]. Why it arises physically is depicted schematically in Figure 2, for the particular case of a stationary mountain wave in the northern winter midlatitude stratosphere. Predominantly eastward winds generate mountain waves propagating westward with respect to this flow, yielding waves with three-dimensional (3D) phase fronts aligned broadly as depicted in Figure 2. Various MLS limb view directions, labeled 1 through 5, are depicted above this wave. Each limb view intercepts the 3D wave structure at the indicated slant and azimuth angle in acquiring saturated radiances from this specific volume of the atmosphere. MLS view direction 1-3 in Figure 2 are the most favorable for resolving this wave, since they intercept the wave roughly parallel to its sloping 3D wave fronts, whereas views 4-5 sample it at progressively more antiparallel alignments with respect to wave phase, which smears the wave's signature out along the limb. For north yaw cycles, MLS views towards the east during descending orbits, yielding viewing geometries somewhat like those labeled 1 and 2 in Figure 2, whereas ascending orbits produce westward MLS view directions and unfavorable viewing geometries more like those labeled 4-5 in Figure 2. For further illustrations of these effects, see *Jiang et al.* [2003a].

[Insert Figure 2 here]

For these reasons, we focus primarily on $(\tilde{\sigma}_A^2)_{ND}$ in our initial investigation of possible mountain wave signals in MLS northern hemispheric radiances. However, this simple ND/NA discrimination is just the first step in unraveling the complex ways in

which MLS viewing angles influence the mountain wave content of the $\tilde{\sigma}_A^2$ data. We defer a thorough treatment of these issues to section 4.2 as part of our attempt to model the mountain wave content of both the $(\tilde{\sigma}_A^2)_{ND}$ and $(\tilde{\sigma}_A^2)_{NA}$ data globally.

3.2 Sensitivity to Background Wind Speed

Dotted contours in Figures 1a and 1c show mean horizontal wind speeds from the United Kingdom Meteorological Office (UKMO) assimilations [Swinbank and O'Neill, 1994], averaged for the specific MLS observation days that contributed data to these variances. Figure 1a shows a strong correlation between enhanced $(\tilde{\sigma}_A^2)_{ND}$ and strong stratospheric horizontal wind speeds U that has been noted in previous studies [e.g., Wu and Waters, 1996a,b; 1997; Jiang and Wu, 2002]. Regions in Figure 1a where U is less than $\sim 10 \text{ m s}^{-1}$ correspond to very small $(\tilde{\sigma}_A^2)_{ND}$ (mainly blue contours where radiance variances are $< 0.01 \text{ K}^2$). Conversely, regions of largest $(\tilde{\sigma}_A^2)_{ND}$ all occur in mid-to-high latitude regions where mean stratospheric winds U are $\sim 25 \text{ m s}^{-1}$ or greater. These $(\tilde{\sigma}_A^2)_{ND}$ enhancements follow to some extent the zonal modulation of the flow by the climatological quasi-stationary wavenumber-1 pattern that emerges in these UKMO wind averages, such that strong (weak) mid-latitude mean winds over Eurasia (North America) correspond to similarly strong (weak) $(\tilde{\sigma}_A^2)_{ND}$ over each continent.

Alexander [1998] showed that the primary source of this U - $(\tilde{\sigma}_A^2)_{ND}$ correlation is the refraction of GW vertical wavelengths by background winds, coupled with the deep vertical width of MLS weighting functions [Wu and Waters, 1997] which do not allow

MLS to resolve GWs with vertical wavelengths $\lambda_z \leq 10\text{km}$ or so. For the specific case of stationary hydrostatic mountain waves, the vertical wavelength λ_z is given by:

$$\lambda_z = \frac{2\pi U \cos \theta}{N} \quad (3)$$

where N is the Brunt-Väisälä frequency and θ is the angle between the horizontal wind U and the wave's horizontal wavenumber vector \vec{K}_h (see, e.g., Figure 2). At latitudes $\sim 40^\circ$ - 60°N over central Eurasia, $U \sim 40$ to 50 ms^{-1} from Figure 1a. If we assume for now that some of these mountain waves are aligned parallel to the mean flow ($\theta \sim 0^\circ$ or 180°), then $N \sim 0.02\text{ rad s}^{-1}$ so that (3) yields $\lambda_z \sim 13\text{-}16\text{ km}$. Thus MLS should resolve these waves, consistent with the variance enhancements observed here in Figure 1a. Conversely, a similar calculation for mountain waves over the Himalayas at $\sim 30^\circ\text{N}$, where $U < 10\text{ ms}^{-1}$, yields $\lambda_z \leq 3\text{ km}$, a vertical wavelength too short for any MLS channel to resolve.

3.3 Enhanced $(\tilde{\sigma}_A^2)_{ND}$ over Mountainous Regions

The analysis in sections 3.1 and 3.2 has introduced some important ways in which mountain waves may and may not manifest in MLS limb track radiances. With these issues in mind, we now compare Figures 1a and 1b and identify four geographical “focus regions” with significant underlying topography where enhanced stratospheric $(\tilde{\sigma}_A^2)_{ND}$ levels are evident. We choose these particular regions based on previous observational precedents for supposing that these variance enhancements are good potential candidates for a mountain wave explanation.

- *Kjønås Mountains of Scandinavia* ($\sim 20^\circ\text{E}$, 65°N): clear $(\tilde{\sigma}_A^2)_{ND}$ bursts are evident in Figure 1a along the northern and southern ends of these mountains. Regional

observations and modeling studies have shown that eastward flow from the Arctic Ocean across these mountains during winter can generate stratospheric mountain waves with long horizontal and vertical wavelengths [e.g., *Dörnbrack et al.*, 2002] that should theoretically be detectable in satellite limb radiances. To study MLS variances here further, we define a latitude-longitude box of 55°-70°N, 5°-40°E.

- *Central and Western Eurasia* (~100°E, 50°N): large geographically-extended $(\tilde{\sigma}_A^2)_{ND}$ values occur in this region where a broad complex of interconnected mountain ranges exist: the Altai, Hangay and Sayan Mountains to the west, the Yablonovyy, Khingan, and Stanavoy Ranges to the east. *Eckermann and Preusse* [1999] noted stratospheric variance enhancements in a similar location during CRISTA infrared stratospheric limb observations in November, 1994, and used the MWFM (see section 4.1) to identify them as stratospheric mountain waves forced by flow across these ranges. We define a latitude-longitude box in the range 45°-65°N, 80°-130°E to study variances in this region further.
- *Queen Elizabeth Islands* (~270°E, 70°N): these Canadian Arctic islands include regions of significant topography, such as Baffin and Ellesmere Islands, the latter slightly poleward of the most northern observing latitudes for saturated MLS radiances. Accumulated high-resolution lidar and balloon profiling of the winter stratosphere over stations in this region has revealed gravity waves whose temperature variances vary in intensity with background winds in ways consistent with quasi-stationary phase speeds, and thus wave energy here has been attributed mostly to locally-generated mountain waves [e.g., *Whiteway and Duck*, 1996,

1999; Duck *et al.*, 1998; Duck and Whiteway, 2000]. For further study of $(\tilde{\sigma}_A^2)_{ND}$ over these islands, we define a latitude-longitude box in the range 65°-75°N, 80°-120°W.

- *Southern Greenland* (~315°E, 65°N): in addition to the large ice cap which dominates Greenland's topographic relief, significant nunataks (mountains that protrude through glacial ice) occur all along the east coast to its southernmost tip. An ER-2 flight over southern Greenland on January 6, 1992 recorded enhanced velocity fluctuations in the stratosphere, which Leutbecher and Volkert [2000] simulated with a mesoscale model and attributed to mountain waves forced by flow over southern Greenland's topography. To study $(\tilde{\sigma}_A^2)_{ND}$ in this region further, we define we define a latitude-longitude box in the range 55°-70°N, 20°-60°W.

In studying $(\tilde{\sigma}_A^2)_{ND}$ variability further over our four mountainous focus regions defined above, we fold in limb-scan data in addition to limb-track data. UARS MLS acquired ~ 6 years of limb-scan data (1991-1997) in addition to the ~3 years of limb-track data (1994-1997). The differences between limb-scan and limb-track data are mainly in viewing geometry and sampling periods [McLandress *et al.*, 2000; Jiang *et al.*, 2003a]. The different viewing geometries give rise to systematic differences in the radiance variances computed from each data type. For example, 4-point and 6-point limb-scan variances are generally much larger than corresponding 6-point limb-track variances, which McLandress *et al.* [2000] attributed to aliasing of longer wavelength GWs into limb-scan data due to a varying LOS angle.

3.3.1 Seasonal and Interannual Variations

Figure 3 plots time series of $(\tilde{\sigma}_A^2)_{ND}$ for channels 1/15, 3/13 and 5 (pressure altitudes $z \sim 28\text{km}$, $\sim 38\text{km}$ and $\sim 48\text{km}$, respectively) over our four mountainous areas of interest: limb-scan variances are shown in panels (a)-(c), limb-track variances in panels (d)-(f). At all four locations we find a strong reproducible annual cycle, peaking in winter.

[Insert Figure 3 here]

Rocket measurements of stratospheric GW temperature variances at middle and high northern latitudes also show annual variations peaking in winter [e.g., *Hirota and Niki*, 1985; *Eckermann et al.*, 1995], as do GPS/MET satellite measurements [*Tsuda et al.*, 2000]. At high latitudes, *Eckermann* [1995] showed that a seasonal variation in atmospheric densities at a given geometric altitude could reproduce most of the observed annual cycle in the rocket data. As noted by *Alexander* [1998], a similar model cannot explain the annual variations of $(\tilde{\sigma}_A^2)_{ND}$ in Figure 3, since MLS channel altitudes are registered at pressure heights rather than geometric heights, which largely factors out the seasonal density effect. Using a ray model, *Alexander* [1998] attributed much of the annual variability in MLS variances to seasonal variations in stratospheric winds that allowed more waves in winter to attain long vertical wavelength and become visible to MLS, in the manner outlined in section 3.2.

In their study of MLS variances over the southern Andes, *Jiang et al.* [2002] also found an annual variation, peaking in winter, which they attributed via modeling studies to increased mountain wave activity in winter. The variance enhancements observed at our four northern hemisphere focus regions also occur during winter and persist into early spring, abating rapidly in April. Very similar winter-to-spring variations have been

observed in stratospheric GWs profiled at stations in and around the Queen Elizabeth Islands, where enhanced winter variances correlate with strong eastward vortex winds [e.g., *Whiteway*, 1999; *Whiteway and Duck*, 1999]. Sudden reductions in early spring occur with final breakdown of the winter vortex, which yields weaker winds and reduced transmission of locally generated mountain waves into the stratosphere [*Duck and Whiteway*, 2000]. Much reduced variances in summer are consistent with westward flow which prevents mountain wave penetration into the middle stratosphere via critical-level filtering. We also note considerable site-to-site and interannual variability of the wintertime peaks in Figure 3, which is consistent with the interannual variability of the winter vortex which gives rise to considerable interannual variations in the intensity of Arctic mountain waves entering the stratosphere [*Dörnbrack and Leutbecher*, 2001]. However, larger limb-scan variances after 1995 are an observational artifact corresponding to changes from “normal scan” mode (top to bottom) to “reverse scan” mode (bottom to top), the latter yielding generally larger $(\tilde{\sigma}_A^2)_{ND}$ variances.

In summary, time series of $(\tilde{\sigma}_A^2)_{ND}$ in Figure 3 are consistent with increases in resolved stratospheric mountain wave over the four focus regions during winter. This interpretation is not definitive, however, since complex wind-modulated visibility effects outlined in section 3.2 yield a similarly phased annual variation [*Alexander*, 1998]

3.3.2 ND versus NA Variances

As noted in section 3.1, mountain waves in winter should manifest more strongly in $(\tilde{\sigma}_A^2)_{ND}$ relative to $(\tilde{\sigma}_A^2)_{NA}$. Figures 1a and 1c showed that, climatologically, mean ND limb-track variances in northern winter were indeed significantly larger than the NA variances over most mountainous regions. To study this in more depth, Figure 4 shows

scatterplots of daily mean ND versus NA limb-scan variances over our four mountainous regions of interest during winter months from 1991-97. When variances are strongly enhanced (i.e. $\gg 0.02 \text{ K}^2$), we note a much greater likelihood that this enhanced variance is observed during ND views, whereas NA views of the same region yield moderate or small variances. This bias is consistent with what we would expect if MLS fluctuations over these regions were enhanced by viewing large-amplitude mountain waves propagating southwestward in a mainly eastward winter stratospheric flow (as depicted in Figure 2).

[Insert Figure 4 here]

3.3.3 Height Variations

Figure 5 plots mean altitude profiles of limb-scan $(\tilde{\sigma}_A^2)_{ND}$ normalized by mean radiance brightness temperatures, derived from the 6 years of measurements in all channels above the four mountainous focus regions during winter. These regional profiles resemble zonal-mean profiles at high latitudes reported in previous studies [*Wu and Waters*, 1996b; *Wu and Jiang*, 2002]: specifically, exponential growth up to an altitude $\sim 50 \text{ km}$, then an apparent “saturation” of the variance profile at altitudes above 50 km. Values here are somewhat smaller than those reported by *Wu and Waters* [1996b] due to a 4-point rather than 6-point variance calculation.

[Insert Figure 5 here]

Wu and Waters [1996b, 1997] interpreted variations below 50 km in terms of the $\sim \exp\left(\int dz / H_E\right)$ growth in wave-induced temperature variances with height [*Fritts and VanZandt*, 1993; *Eckermann*, 1995; *Fritts and Alexander*, 2003]. When $H_E \approx H_\rho \approx 7 \text{ km}$ (where H_ρ is density scale height), all the waves are nondissipating: growth at this rate is

shown with a grey curve in Figure 5. “Energy scale heights” H_E for the MLS variances below ~ 50 km in Figure 5 are ~ 12 km, suggestive of some limited dissipation of wave energies with height.

Above ~ 50 km, variances in Figure 5 become almost constant with height ($H_E \rightarrow \infty$). Two interpretations of this observation have been proposed. *Wu and Waters* [1996b, 1997] interpreted this as a transition to greater GW dissipation, leading to saturation limits at high altitudes indicative of strong wave breaking. *Wu and Jiang* [2002] reiterated this interpretation when studying variances over Antarctica, while *Wu* [2001] proposed a similar explanation for vertical growth tendencies observed in along-track wavenumber spectra of MLS radiances. *Alexander* [1998], however, used a global GW model to argue that wind-modulated MLS visibility effects in section 3.2 produced most of the apparent “saturation” in variances above 50 km, and that profiles like those in Figure 5 gave little indication of where the strongest wave breaking was occurring.

We leave these interpretation issues for further dedicated modeling studies. Here, we point out that the vertical variations of MLS variances over these four mountainous locations are generally consistent with earlier zonal mean results and indicate that the GW activity here propagates through the stratosphere and into the mesosphere. This is consistent with a mountain wave interpretation, since eastward winter stratospheric flow persists climatologically into the lower mesosphere and so should often allow mountain waves to propagate through the full depth of the winter middle atmosphere from 0-50 km. The strong altitude correlations between winter variance enhancements in Figure 3 further support such conclusions.

4. MWFM Modeling of Mountain Waves in MLS Variances

Data analysis in section 3 has provided evidence that mountain waves may be enhancing $(\tilde{\sigma}_A^2)_{ND}$ variances over topography. To investigate these issues in depth, we develop here a global modeling strategy for estimating the mountain wave content of MLS radiances using the Mountain Wave Forecast Model (MWFM). We begin by briefly introducing the MWFM, develop in detail a critical “MLS visibility function,” which specifies the waves that MLS can and cannot see in orbit, and then apply it to some simple examples. Finally we outline details of our MWFM simulations with this visibility term included that are targeted to the MLS observations presented in section 3.

4.1 The Mountain Wave Forecast Model (MWFM)

Bacmeister et al. [1994] documents the first version of this model (MWFM-1). Here, as in *Jiang et al.* [2002], we use version 2 (MWFM-2). The MWFM uses a set of diagnosed quasi-two dimensional (2D) ridge functions that fit the dominant features in the Earth's topography relevant for mountain wave generation [*Bacmeister et al.*, 1994]. Each ridge function has a range of properties: the most important are its geographical location, cross-ridge width L , peak height h , base altitude z_b and horizontal orientation ϕ_{LONG} of its long (along-ridge) axis. Also important for MWFM-2 calculations is a normalized “ridge quality” parameter q ($0 \leq q \leq 1$), which defines how closely the original topography was approximated by fitting a 2D ridge function: $q \sim 1$ indicates highly 2D ridge-like topography, whereas $q \ll 1$ usually indicates a more symmetric three-dimensional (3D) obstacle.

The model ingests forecast or analyzed wind fields and “blows” the local winds at the base altitude z_b of the ridge across it to generate a source-level mountain wave field.

MWFM-2 models forced mountain wave fields using a nonhydrostatic three-dimensional spatial ray-tracing formulation with Coriolis and stratification terms included [Marks and Eckermann, 1995], constrained by a uniformly stationary ground-based phase speed for each ray. A series of rays are launched from the parent ridge with a given horizontal wavenumber vector $(\vec{K}_h)_i$ directed at I_ϕ different equispaced azimuth angles ϕ_i that span the 180° range $\phi_{OR} - 90^\circ \leq \phi_i < \phi_{OR} + 90^\circ$, where ϕ_{OR} is the azimuth orthogonal to the long axis of the ridge ($\phi_{OR} = \phi_{LONG} \pm 90^\circ$) and i is an integer that labels each ray ($i = 1 \dots I$).

Rays aligned parallel to ϕ_{OR} are forced with the largest peak vertical-displacement amplitude based on the peak ridge height h . The ridge quality q is used to scale wave amplitudes down from this value as a function of displacement of the ray azimuth from ϕ_{OR} , $|\phi_i - \phi_{OR}|$. For $q \sim 0$ (quasi-3D obstacle), the amplitude reduction as a function of $|\phi_i - \phi_{OR}|$ is small, whereupon the multiray method often yields three-dimensional “ship wave” patterns radiating from the obstacle as rays at various azimuths radiate obliquely away from the source with significant amplitudes [see, e.g., Gjevik and Marthinsen, 1978; Broutman et al., 2001]. For $q \sim 1$ (2D ridge-like topography), initial wave amplitudes decay rapidly with increasing $|\phi_i - \phi_{OR}|$, and thus the ray method yields significant energy only for those few rays aligned close to ϕ_{OR} , yielding a plane wave pattern with phase lines quasi-parallel to the long ridge axis, much as is observed for flows over two-dimensional ridges. Once assigned, these wave amplitudes vary along each ray’s group propagation path according to conservation of the vertical flux of wave action density, subject to dissipation by dynamical and convective wave breaking

thresholds [Marks and Eckermann, 1995]. Wave breaking is parameterized using a linear saturation hypothesis, with wave action densities scaled back accordingly. At any altitude the wave action density can be converted to a more usual wave amplitude measure [Marks and Eckermann, 1995]. In these experiments we convert to peak temperature amplitude \hat{T}_i , which relates most closely to the radiance fluctuations measured by MLS.

The total number of rays launched from each ridge $I = I_K I_\varphi$, where I_K is the total number of horizontal wavenumbers assigned to each ridge and I_φ is the total number of propagation azimuths per horizontal wavenumber. In the experiments reported here, $\left|(\vec{K}_h)_i\right| = (K_h)_i = 1.5 j_i / L$ ($j_i = 1 \dots I_K$, L is cross ridge width), $I_K = 2$ and $I_\varphi = 18$, yielding a total of 36 rays per ridge. Since we ignore horizontal gradient terms in our ray formulation, these source-level horizontal wavenumbers and azimuths remain constant along each ray trajectory.

In the MWF2 we use the sign convention of Eckermann [1992]. We define $m < 0$ for upward propagating mountain waves. For the horizontal wavenumber vector $(\vec{K}_h)_i = (k_i, l_i) = (K_h)_i (\cos \varphi_i, \sin \varphi_i)$, we define the absolute wavenumber azimuth φ_i such that the component of $(\vec{K}_h)_i$ in the direction of the background horizontal wind vector $\vec{U} = (U, V) = U_h (\cos \chi, \sin \chi)$ is always negative. This always yields $(\vec{K}_h)_i \cdot \vec{U} < 0$ and thus positive intrinsic frequencies $(\omega_i = -(\vec{K}_h)_i \cdot \vec{U} > 0)$, so that the intrinsic vertical phase velocity $\omega_i / m_i < 0$ and thus phase moves downwards for waves propagating energy upwards. Further, intrinsic horizontal phase speed along the horizontal wind vector direction is $\omega_i / [(K_h)_i \cos(\varphi_i - \chi)] = -U_h$, which has the mountain wave

propagating it's phase in the intrinsic frame away from the wind at the same speed as the wind, so that phase in the ground-based frame is always stationary, as required.

This consistent sign convention proves particularly important for quantifying the precise sensitivity of MLS to MWFM-simulated mountain waves, as will now be described.

4.2 MLS analytical filter function and implementation in MWFM

The MWFM generates mountain waves with a broad range of possible vertical and horizontal wavelengths, yet, as noted in sections 3.1 and 3.2, MLS can only resolve a small subset of these waves. To enable meaningful MWFM-MLS comparisons, we must apply an observational filter to the MWFM results that accurately specifies the sensitivity of MLS to mountain waves of various horizontal and vertical wavelengths aligned at various angles to the MLS LOS.

In earlier MWFM modeling of MLS variances over the Andes, *Jiang et al.* [2002] adopted a simple filter that retained waves with vertical wavelengths $\lambda_z > 10$ km and horizontal wavelengths $\lambda_h > 30$ km, similar to the earlier modeling approach of *Alexander* [1998]. However, on hemispheric scales, *Wu and Waters* [1997] and *McLandress et al.* [2000] showed that there was an important azimuthal sensitivity to the MLS response which changed as the MLS viewing angle changed from the bottom (top) to the top (bottom) of any given ascending (descending) orbital segment. *McLandress et al.* [2000] derived an analytical observational filter function for MLS limb track observations, which approximated the global three-dimensional response to gravity waves. In order to simulate how MWFM-simulated mountain waves in the NH winter stratosphere manifest in MLS data, we developed a fairly general MLS filter function that builds upon this existing work, and implemented it within the MWFM. Given its important role in model-

data comparisons, a full description follows. We do not derive a similar filter function for the limb scan data here: as noted by *McLandress et al.* [2000], additional complications (e.g., variable LOS) makes analytical treatment of the limb scan response considerably more difficult.

Figure 6 shows the horizontal geometry of the MLS observation for a descending orbital segment. Given our focus on ND variances $(\tilde{\sigma}_A^2)_{ND}$, we consider the north/descending MLS view, shown in darker colors on the top-right. MLS limb-track radiances for this channel saturate at an altitude z_C : for channels 3 and 13, $z_C = 38$ km and the tangent height $z_t = 18$ km [*Wu and Waters*, 1997]. The portion of the atmosphere centered at z_C contributes most to the retrieved MLS radiance, and so we define this as the instantaneous “data point” and the line of data points acquired following the satellite motion as the “data track”. We define (x,y,Z) axes with the origin at the data point, such that $Z = z - z_C$ where z is height above the Earth’s surface. As in *McLandress et al.* [2000], we specify the instantaneous horizontal viewing geometry in terms of the horizontal azimuth angle α_T of the orbital motion vector from due east, and then rotate the (x,y,Z) axes by this angle to new axes (X,Y,Z) such that satellite motion now occurs along the X axis and MLS views the atmospheric limb along the Y axis, at 90° to the spacecraft motion, as depicted in Figure 6:

$$\begin{pmatrix} X \\ Y \\ Z \end{pmatrix} = \begin{pmatrix} \cos \alpha_T & \sin \alpha_T & 0 \\ -\sin \alpha_T & \cos \alpha_T & 0 \\ 0 & 0 & 1 \end{pmatrix} \begin{pmatrix} x \\ y \\ z - z_C \end{pmatrix} \quad (4)$$

[Insert Figure 6 here]

Figure 7 plots track angles α_T as a function of latitude for both ascending and descending orbits and for the two yaw cycles where MLS points either to the north or to

the south. For south viewing geometries, we adopt a slightly different definition of α_T from *McLandress et al.* [2000], such that the values we use are 180° different. The UARS yaw maneuver is succinctly described by a reflection of the Y axis about the X axis (see Figure 6), the convention used by *McLandress et al.* [2000]. However, this has the disadvantage of transforming the (X,Y) axes from right-handed to left-handed [Anton, 2000] which complicates sign conventions for gravity wave wavenumbers. To get around this, our approach here is to treat the yaw maneuver as a 180° rotation of the (X,Y) coordinate axes. The advantage is that this and all subsequent axis transformations are rotations and so right-handed coordinate axes persist throughout. The disadvantage is that the X axis is rotated such that, for southern views, the satellite motion is in the negative direction along the X axis, rather than in the positive direction specified in the original α_T definition. The MLS visibility functions introduced below prove insensitive to the absolute sense of quantities along the X axis, so for our purposes this side effect poses no problems.

[Insert Figure 7 here]

The MLS view along the Y axis points downward through the atmosphere at an angle β with respect to the horizontal plane, where by geometry (see Figure 11b of *McLandress et al.*, 2000)

$$\beta = -\cos^{-1}[(a + z_t)/(a + z_c)] \quad (5)$$

and the radius of the Earth $a=6378$ km. For channels 3 and 13, $\beta = -4.53^\circ$ and thus this small angle allows us to assume $\sin\beta \approx \beta$ to a good approximation.

The vertical temperature weighting functions for each MLS channel [*Wu and Waters*, 1996b] are approximated using the Gaussian fit

$$W_z(Z) = \exp\left[-\left(\frac{Z}{w_c}\right)^2\right] \quad (6)$$

where $w_c \approx 6.8$ km for channels 3 and 13 [McLandress *et al.*, 2000], as plotted in Figure 8b. The width of the MLS antenna pattern yields additional smearing across the MLS line of sight (LOS) in the Y - Z plane. On ignoring the small increases in this spatial width with increasing Y , this across-LOS weighting function at the data point can be approximated as

$$W_{LOS}(Y, Z) = \exp\left[-\left(\frac{Z - Y\beta}{w_b}\right)^2\right] \quad (7)$$

where by geometry the antenna's full width half maximum (FWHM) of $\sim 0.206^\circ$ [Jarnot *et al.*, 1996] corresponds to $w_b \approx 4.85$ km for channels 3 and 13. This function is plotted in Figure 8a, and shows the MLS LOS at an angle β below the horizontal and the symmetric response around this LOS due to the antenna width. The net weighting function along the (Y, Z) plane, centered about the data point, is the product of (6) and (7):

$$W_{YZ}(Y, Z) = W_z(Z)W_{LOS}(Y, Z) \quad (8)$$

which is plotted in Figure 8c.

[Insert Figure 8 here]

The along-track (X) weighting function is determined by a somewhat broader antenna width of $\sim 0.43^\circ$ (FWHM) in this direction [Jarnot *et al.*, 1996], which can be approximated as

$$W_x(X) = \exp\left[-\left(\frac{X}{w_s}\right)^2\right] \quad (9)$$

where $w_s \approx 10.1$ km for channels 3 and 13 [McLandress *et al.*, 2000]. Not considered in (9) is an additional along-track broadening due to the 2s integration time for each MLS

measurement, which, given the 7.5 km s^{-1} satellite velocity, corresponds to a 15 km footprint along-track. We modeled this effect numerically, and found that it led to a broadened normalized Gaussian that was well fitted by (9) but using $w_s \approx 12 \text{ km}$.

Thus the three-dimensional (3D) MLS weighting function about the data point is

$$W(X, Y, Z) = W_X(X)W_{YZ}(Y, Z) \quad (10)$$

Equations (6)-(8) can be re-expressed by rotating axes by an angle

$$2\phi = \tan^{-1} \left[\frac{2\beta}{1 - \beta^2 + \gamma^{-1}} \right] \quad (11)$$

such that

$$\begin{pmatrix} X' \\ Y' \\ Z' \end{pmatrix} = \begin{pmatrix} 1 & 0 & 0 \\ 0 & \cos \phi & \sin \phi \\ 0 & -\sin \phi & \cos \phi \end{pmatrix} \begin{pmatrix} X \\ Y \\ Z \end{pmatrix} \quad (12)$$

This transformation enables (8) to be re-expressed as a separable two-dimensional (2D) weighting function [McLandress *et al.*, 2000]

$$W_{YZ}(Y, Z) \rightarrow W_{YZ'}(Y', Z') = \exp \left[-\left(\frac{Y'}{w_{Y'}} \right)^2 \right] \exp \left[-\left(\frac{Z'}{w_{Z'}} \right)^2 \right] \quad (13)$$

where

$$\begin{aligned} w_{Y'} &= \frac{w_C}{\left[\sin^2 \phi + \gamma (\sin \phi - \beta \cos \phi) \right]} \\ w_{Z'} &= \frac{w_C}{\left[\cos^2 \phi + \gamma (\cos \phi + \beta \sin \phi) \right]} \end{aligned} \quad (14)$$

The cigar-shaped MLS weighting function in Figure 8c has a major axis that is aligned at an “effective line of sight” angle ϕ that is more horizontal than the actual MLS LOS angle β , as was noted in earlier studies [e.g., Figure 6b of Wu and Waters, 1997]. The angle ϕ quantifies this effective LOS: $\phi \sim -2.94^\circ$ for channels 3 and 13.

The separable 3D MLS weighting function $W'(X, Y', Z') = W_X(X)W_{YZ'}(Y', Z')$ represents a point spread function about the atmospheric data point to be measured. This point spread function (or instrument function) will be convolved through the spatially varying atmospheric temperature field, $T(X, Y', Z')$, as the satellite moves along the X axis acquiring atmospheric radiances along the limb track. The Fourier transform of $W'(X, Y', Z')$ is

$$\begin{aligned} R(k_X, k_{Y'}, k_{Z'}) &= R_X(k_X)R_{Y'}(k_{Y'})R_{Z'}(k_{Z'}) \\ &= \exp\left[-(\pi w_X k_X)^2 - (\pi w_{Y'} k_{Y'})^2 - (\pi w_{Z'} k_{Z'})^2\right] \end{aligned} \quad (15)$$

where k_X , $k_{Y'}$ and $k_{Z'}$ are wavenumbers (in cyc km^{-1}) along the X , Y' and Z' axes, respectively. Since convolution of $W'(X, Y', Z')$ with $T(X, Y', Z')$ in the spatial domain corresponds the multiplication of the same quantities in the Fourier domain, then $R(k_X, k_{Y'}, k_{Z'})$ represents the spectral sensitivity or “visibility” [Kraus, 1996] of the MLS instrument to temperature structure of a spatial scale defined by the three-dimensional wavenumber $(k_X, k_{Y'}, k_{Z'})$, such that

$$\begin{pmatrix} k_X \\ k_{Y'} \\ k_{Z'} \end{pmatrix} = \begin{pmatrix} 1 & 0 & 0 \\ 0 & \cos \phi & \sin \phi \\ 0 & -\sin \phi & \cos \phi \end{pmatrix} \begin{pmatrix} k_X \\ k_Y \\ k_Z \end{pmatrix} \quad (16)$$

where k_Y and k_Z are wavenumber components (in cyc km^{-1}) along the Y and Z axes. For a gravity wave with a wavenumber vector $\vec{K} = (k, l, m)$ defined along the usual (x, y, z) axes,

such that $\vec{K}_h = (k, l) = K_h(\cos \phi, \sin \phi)$ where $K_h = (k^2 + l^2)^{1/2}$, then

$k_X = K_h \cos[\phi - \alpha_T]$, $k_Y = K_h \sin[\phi - \alpha_T]$, and thus

$$\begin{pmatrix} k_X \\ k_Y \\ k_Z \end{pmatrix} = \begin{pmatrix} \cos \alpha_T & -\sin \alpha_T & 0 \\ \sin \alpha_T & \cos \alpha_T & 0 \\ 0 & 0 & 1 \end{pmatrix} \begin{pmatrix} k \\ l \\ m \end{pmatrix} \quad (17)$$

Thus (16) and (17) transform us from/to the 3D gravity wave wavenumber (k, l, m) to/from the components $(k_X, k_{Y'}, k_{Z'})$ relevant to the MLS visibility calculation (15).

The sign of the GW wavenumbers (k, l, m) must be defined self-consistently to properly represent via (17) the precise 3D wave orientations that MLS is most sensitive to. The MWFM ray-tracing sign convention for mountain waves described in section 4.1 fulfills these requirements.

Figure 9b plots the two-dimensional (2D) MLS spectral visibility function $R_{YZ'}(k_{Y'}, k_{Z'}) = R_{Y'}(k_{Y'})R_{Z'}(k_{Z'})$ in (k_Y, k_Z) space following application of the inverse of the transformation (16). The tilted nature follows directly from the tilt of $W_{YZ}(Y, Z)$ about the ϕ axis in Figure 8c. Also plotted are the lines $k_Y = -k_Z \sin \phi$ (solid grey) and $k_Y = -k_Z \sin \beta$ (dotted grey), which, for a given contour level, mark the shortest vertical wavelength λ_Z and along-track wavenumber λ_Z , respectively, that yield an MLS visibility of a given level or greater at some altitude. For example, on inspecting Figure 9b we can see that the wave with the shortest across-track horizontal wavelength resolved at the 40% level (where the dotted line intercepts the 0.4 contour) is ~ 200 km with a corresponding vertical wavelength of $\sim (200 \text{ km})/|\sin \beta| \sim 16$ km. The shortest vertical wavelength resolved at the 40% level is ~ 13 km with a corresponding across-track wavelength of $\sim 13|\sin \phi| \text{ km} \sim 250$ km.

[Insert Figure 9 here]

We see from Figure 9b that the peak response for upward-propagating waves ($m < 0$, hence $k_Z < 0$) occurs for waves with $k_Y < 0$. As noted by *McLandress et al.* [2000], this occurs because in this case the gravity wave phase lines are quasi-parallel to the MLS LOS β and effective LOS ϕ , and thus the wave presents a rotated wavenumber $k_{Y'} \sim 0$ to

MLS, optimizing its visibility (as depicted schematically for view 2 in Figure 2). In other words, MLS is more sensitive to gravity waves that are propagating in the intrinsic frame towards the instrument, i.e., in the negative direction along the Y' axis depicted in Figure 6.

4.3 GWs resolved in MLS 6-point limb-tracking variances

Given the complex three-dimensional nature of the MLS visibility function, we first apply these analytical relations to single monochromatic plane waves to assess in simple illustrative terms the types of gravity waves we might expect to resolve in the MLS 6-point variances. The along-track spectral visibility $R_X(k_X)$ is plotted with the thick dark grey curve in Figure 9a. The 2s MLS integration time means that data are acquired every 15 km along track, and so the Nyquist along-track wavelength $(\lambda_X)_{\text{short}}=30$ km. The 6 point data segments yield a longest (fundamental) along-track wavelength $(\lambda_X)_{\text{long}}=90$ km. We approximate waves resolved along-track for now by cutting off the $R_X(k_X)$ response at $(\lambda_X)_{\text{short}}$ and $(\lambda_X)_{\text{long}}$, as shown with the light grey solid curve in Figure 9a.

$(\lambda_X)_{\text{long}}=90$ km represents the longest gravity wave horizontal wavelength that is fully resolvable in the 6-point MLS variances. A wave of $(\lambda_X)_{\text{long}}=90$ km is only visible to MLS when it propagates directly along the X axis, since propagation in any other direction leads it to project a longer wavelength component along the X axis, and thus it gets filtered out following the long wavelength cutoff in Figure 9a.

To study the directional sensitivity to waves in this 30-90 km horizontal wavelength band more quantitatively, we consider a specific example: a gravity wave of horizontal wavelength $\lambda_h = K_h^{-1} = 80$ km and vertical wavelength $\lambda_z=20$ km. We profile this wave's MLS visibility (15) in Figure 10 as a function of latitude and wave propagation azimuth

φ for north-descending (ND) orbits: the track angles α_T as a function of latitude are overplotted from Figure 7 with the broken grey curve.

[Insert Figure 10 here]

We see that nonzero MLS visibilities only occur for propagation azimuths φ near $\alpha_T + 180^\circ$, indicating that MLS is primarily sensitive to this wave when it propagates in the along-track (X) direction, as then it projects long across-track wavelengths that are not smeared out along the limb. However, the peak response (red) is offset from α_T by $\sim 12^\circ$ in this case. The reason for this can be gleaned from Figure 9b, which shows that the peak visibility for a given vertical wavelength is located along the grey solid curve $k_Y/k_Z = -\sin \phi$. Since $k_Y = K_h \sin(\varphi - \alpha_T)$ for a given gravity wave, then the peak response comes from equating these two equations:

$$\sin(\varphi - \alpha_T) = \frac{\lambda_h \sin \phi}{\lambda_Z} \quad (18)$$

For channels 3/13 ($\phi = -2.93^\circ$), this yields $\varphi - \alpha_T \approx -12^\circ$. Note from (18) that this offset scales as λ_h/λ_Z , and thus the maximum absolute offset in the peak response from α_T is defined by the maximum value of λ_h/λ_Z . Since the visibility in Figure 9b is $< 20\%$ for all waves with λ_Z less than ~ 10 km, we set $(\lambda_Z)_{\min} = 10$ km and note that $(\lambda_h)_{\max} = (\lambda_X)_{\text{long}} \cos(\varphi - \alpha_T)$, where $(\lambda_X)_{\text{long}} = 90$ km. Substituting this into (18) yields

$$\tan(\varphi - \alpha_T)_{\max} = \frac{(\lambda_X)_{\text{long}} \sin \phi}{(\lambda_Z)_{\min}} \quad (19)$$

Since $(\lambda_X)_{\text{long}}/(\lambda_Z)_{\min} = 9$, (19) yields a maximum absolute offset $(\varphi - \alpha_T)_{\max} \approx -25^\circ$ for the peak wave response in channels 3/13. Thus the peak responses of all the waves resolved in the 6-point variances are clustered at wave propagation azimuths φ which are

less than 25° away from the track angle α_T . Note too that for all resolved waves the ratio $\lambda_h/\lambda_z < 9$ which, from the hydrostatic dispersion relation, implies that waves resolved in MLS data generally have high intrinsic frequencies [Alexander, 1998; McLandress et al., 2000].

Figure 10 also shows a sharp cutoff in visibility from values of ~ 0.2 to zero at angles $\varphi - \alpha_T \approx -30^\circ$. This corresponds to the onset of the long wavelength along-track filter at $\lambda_X > (\lambda_X)_{long} = 90$ km as depicted in Figure 9a: since $\lambda_X = \lambda_h \cos(\varphi - \alpha_T)$ and $\lambda_h = 80$ km, λ_X exceeds 90 km and the wave is filtered out when $(\varphi - \alpha_T) < -27^\circ$.

The sharp long wavelength cutoff at $(\lambda_X)_{long} = 90$ km in Figure 9a is a coarse initial approximation. To delineate the true nature of the long wavelength response, we conducted numerical simulations in which a randomly phased gravity wave of a given along-track wavelength was sampled at 6 successive points every 15 km, then a 6-point variance calculation exactly like that in (1) was performed. In particular, the fitting and removal of the linear trend in (1) modifies the Fourier content of the data and incompletely removes longer wavelength gravity waves. The simulated ratio of retrieved to actual variance from 1000 Monte Carlo simulations for each wavelength is plotted as a function of λ_X in Figure 11 (solid curve). The thick grey curve fits this dependence with the function

[Insert Figure 11 here]

$$f(\lambda_X) = \frac{1 + (\lambda_2 / \lambda_1)^p}{1 + (\lambda_X / \lambda_1)^p} \quad \text{for } \lambda_X \geq \lambda_2 \quad (20)$$

$$f(\lambda_X) = 1 \quad \text{for } \lambda_X < \lambda_2$$

where $\lambda_1=100\text{km}$, $\lambda_2=60\text{km}$ and $p=4.3$. Thus we modify the along-track component of the 3D visibility in (15), $R_X(k_X)$, to yield a new along-track visibility function

$$R'_X(k_X) = R_X(k_X) f^{1/2}(k_X^{-1}) \quad (21)$$

where the square root in (21) reflects the fact that (20) is a variance response, whereas (15) and (21) refer to amplitude sensitivity. The response (21) is plotted as the broken curve in Figure 9a: we note a much more gradual roll-off in the long wavelength response along-track.

Figure 12 summarizes the results of this section with a schematic “polar diagram” of the response of MLS 6-point radiance variances to a gravity wave of a given horizontal wavenumber directed at various azimuths φ . We note primary sensitivity to those waves whose propagation azimuths are aligned along-track, with an offset to waves propagating towards the instrument’s line of sight. This sensitivity is fixed to the (X,Y) axes, which rotate as the track angle α_T varies with latitude and yaw cycle, as depicted in Figures 7 and 10. Referring back to Figure 2, the optimum viewing geometry lies somewhere between MLS view directions 2 and 3. Thus, on ND orbits, MLS 6-point variances $(\tilde{\sigma}_A^2)_{ND}$ resolve zonally propagating waves at the start and end orbit latitudes of $\sim 80^\circ\text{N}$ and $\sim 35^\circ\text{S}$, respectively, peaking for waves with a small southward component to their wave vectors. At mid-orbit latitudes of $\sim 0^\circ\text{-}50^\circ\text{N}$ where $\alpha_T \approx -60^\circ$, and assuming an offset for the polar diagram peak of $(\varphi - \alpha_T) \approx -12^\circ$ for a $\lambda_h = 80\text{ km}$ and $\lambda_z = 20\text{ km}$ wave, the variances are most sensitive to waves propagating at azimuths φ of $\sim -70^\circ$ and 132° , the former directed 18° east of due south, the latter directed 42° west of due north. This narrow bidirectional response of MLS to gravity waves is implicit in earlier modeling results of *McLandress et al.* [2000]: see, e.g., their Figure 14.

[Insert Figure 12 here]

4.4 MWFM Simulations of MLS Variances

In our MWFM modeling of mountain waves in MLS variances, we used temperatures, horizontal winds and geopotential heights from UKMO assimilated meteorological data [Swinbank and O'Neill, 1994], since they issued uninterrupted daily (12Z) analyses over the duration of the UARS mission. These fields are issued on a global $3.75^\circ \times 2.5^\circ$ longitude-latitude grid at 18 standard pressure levels from 1000hPa to 0.4 hPa. We ran MWFM-2 in “hindcast” mode through this analyzed atmosphere over the entire Northern Hemisphere during every MLS observation day for the period 1994-97. Relevant mountain wave ray parameters returned at selected stratospheric pressure level are the wave packet’s geographical location, wavenumber vector and it’s peak temperature amplitude $\hat{T}_i(p)$.

After each hemispheric MWFM-2 forecast, we can process all the ray data through an MLS GW visibility function. For a given mountain wave ray number i that has propagated through the UKMO atmosphere to a pressure level p , where it has a peak temperature amplitude of $\hat{T}_i(p)$, we scale the amplitude according to the MLS GW visibility functions (15) and (21) to a new MLS-measured mountain wave temperature amplitude

$$\hat{T}_i^{MLS}(p) = [R'_X(k_X)R_{Y'}(k_{Y'})R_{Z'}(k_{Z'})]\hat{T}_i(p) \quad (22)$$

Note that the MLS GW visibility term in (22) is a function of the transformed mountain wave wavenumber $(k_X, k_{Y'}, k_{Z'})$, which, from (5), (6), (11), (14), (16), and (17), makes it also an implicit function of observing latitude (MLS LOS), yaw cycle, ascending or

descending orbit and channel number. We concentrate primarily on channels 3 and 13 ($z_c \approx 38$ km) hereafter.

The raw ray data from each hemispheric MWFM-2 forecast are voluminous [see, e.g., *Eckermann and Preusse, 1999; Hertzog et al., 2002*]. Since we must generate and store results from many years of such forecasts, we need to reduce this data volume after each forecast prior to storage. We choose to average the ray data from each daily forecast to derive mean square peak MLS-measured mountain wave amplitudes $\overline{\hat{T}^2}(p)$ within $2.5^\circ \times 2^\circ$ grid boxes at various pressure levels throughout the Northern Hemisphere. We also compute other potentially useful quantities: e.g., standard deviations of the rms MLS-measured temperature amplitude, for potential comparison with standard deviations of MLS radiances derived in previous studies [*McLandress et al., 2000*]. This averaging procedure is similar to the ones performed in some previous MWFM studies [*Jiang et al., 2002; Pierce et al., 2003*].

5. Comparison of MWFM Results with MLS Variances

5.1 MWFM Results without MLS Filtering

Figure 13 plots maps of the gridbox-averaged MWFM mean-square peak mountain wave temperature amplitude, $\overline{\hat{T}^2}(p)$, at 5 hPa ($z \sim 37$ km), the approximate altitude of MLS Channel 3/13 data ($z_c \sim 38$ km). The data are further averaged in time for simulations in all winter months (December-February) over all MLS limb-track observing days during 1994-97. However, no observational filtering of any kind was applied to these data: thus, they represent the full (control) MWFM mountain wave temperature climatology during the MLS limb-track observation period.

[Insert Figure 13 here]

The $\overline{\hat{T}^2}(p)$ maps in Figure 13 show some similarities with the MLS ND radiance variances $(\tilde{\sigma}_A^2)_{ND}$ in Figure 1a. Obvious areas of some correspondence are variance enhancements over Scandinavia, southern Greenland, Iceland, and the northern Urals, immediately suggesting these MLS variance enhancements may be mountain wave-induced. However, in general there are quite significant differences between the MLS ND variances and $\overline{\hat{T}^2}(p)$. Some of the main discrepancies are:

- 1) MWFM simulates enhanced mountain wave activity all along the west coast of North America, from southern Alaska all the way down to Mexico. MLS ND variances $(\tilde{\sigma}_A^2)_{ND}$ show much less activity here.
- 2) $(\tilde{\sigma}_A^2)_{ND}$ in Figure 1a is enhanced over the Queen Elizabeth Islands and northern Alaska, where much less MWFM activity is evident in Figure 13.
- 3) MLS $(\tilde{\sigma}_A^2)_{ND}$ and MWFM $\overline{\hat{T}^2}(p)$ fields both show enhancements across continental Europe, but the geographical distributions are different. For example, the MWFM $\overline{\hat{T}^2}(p)$ values typically maximize $\sim 10\text{-}20^\circ$ further south than $(\tilde{\sigma}_A^2)_{ND}$.
- 4) There is significant MLS ND variance over north-eastern Europe, where MWFM $\overline{\hat{T}^2}(p)$ is much weaker.

One interesting feature of Figure 13 is the almost total absence of significant mean mountain wave temperature amplitudes in the northern equatorial regions ($0\text{-}15^\circ\text{N}$), despite the presence of some significant mountains there (see Figure 1b).

5.2 MWFM Results using MLS ND Filtering

To model $(\tilde{\sigma}_A^2)_{ND}$ (reproduced in Figure 14a to aid visual comparisons), Figure 14b plots 5 hPa MWFM $\overline{\hat{T}_{ND}^2}(p)$ fields: these are the MWFM-generated mean-square peak mountain wave temperature amplitudes after application of the MLS ND GW visibility filter (22). Substantial departures from the unfiltered MWFM control climatology in Figure 13 are evident. The most obvious change is in overall scale: $\overline{\hat{T}_{ND}^2}(p)$ is smaller than $\overline{\hat{T}^2}(p)$ by a factor of $\sim 10^3$. This highlights how most of the simulated waves in Figure 13 are not resolved by MLS.

[Insert Figure 14 here]

The geographical distributions differ considerably too, with $\overline{\hat{T}_{ND}^2}(p)$ showing enhanced variance at higher latitudes than $\overline{\hat{T}^2}(p)$, with little variance evident at latitudes equatorward of $\sim 30^\circ\text{N}$. The specific variance structure in Figure 14b agrees much better with the $(\tilde{\sigma}_A^2)_{ND}$ data. The four specific inconsistencies that were noted between Figures 13 and 1a/14a in section 5.1 are all improved or eliminated:

- 1) The enhanced MWFM mountain wave activity all along the west coast of North America in Figure 13 is substantially suppressed after ND filtering in Figure 14b, and now agrees much better with the $(\tilde{\sigma}_A^2)_{ND}$ data in Figure 14a.
- 2) Greater MWFM activity occurs in Figure 14b over northern Alaska and Baffin Island, in better agreement with the $(\tilde{\sigma}_A^2)_{ND}$ data.

- 3) Geographical variance enhancements in $\overline{\hat{T}_{ND}^2}(p)$ across continental Europe agree better with Figure 14a, with MWFM variance enhancements generally displaced northward.
- 4) Significant MWFM $\overline{\hat{T}_{ND}^2}(p)$ now exists over north-eastern Europe in Figure 14b, as observed in $(\tilde{\sigma}_A^2)_{ND}$ in Figure 14a.

Some differences still exist between Figures 14a and 14b. MWFM activity over the Queen Elizabeth Islands is “spottier” than the extended variance enhancement observed in Figure 14a. Modeled mountain wave activity over the Alps and Atlas Mountains are larger than observed, and there are nearby MLS variance enhancements in Figure 14a away from mountains that are not seen in Figure 14b. There is also enhanced $(\tilde{\sigma}_A^2)_{ND}$ over the Notre Dame/Laurentides mountains whereas MWFM shows weaker activity that extends from the Laurentides down along the Appalachians.

Nonetheless, on the hemispheric scale there is noticeable similarity between the MWFM and MLS maps in Figure 14, with the comparison much improved over the unfiltered control run in Figure 13. Figure 14 leads us to conclude that there is considerable mountain wave information buried within these limb-track MLS ND radiance variances. Combined with the analysis results in sections 3.3.1 and 3.3.2, we feel we can confidently attribute variance enhancements over three of our four focus regions to stratospheric mountain waves: Scandinavia, central Eurasia, and Greenland. Enhancements over the Queen Elizabeth Islands seem to be at least partly mountain wave-related based on our analysis and modeling, though MLS shows greater enhancements than were modeled by the MWFM.

Comparing model and data in Figure 14, we now propose that the following $(\tilde{\sigma}_A^2)_{ND}$ enhancements in Figure 14a are also due to stratospheric mountain waves forced by flow over the following mountainous features, which we list from Figure 1b on progressing from west to east:

- 1) the Alps ($\sim 10^\circ\text{E}$, 45°N)
- 2) northern Ural Mountains ($\sim 60^\circ\text{E}$, 65°N)
- 3) Putoran Mountains ($\sim 95^\circ\text{E}$, 68°N)
- 4) The Altai and Hangay Mountains ($\sim 90^\circ\text{-}100^\circ\text{E}$, $45^\circ\text{-}50^\circ\text{N}$)
- 5) Sayan Mountains and Yablonovyy Ranges ($\sim 95\text{-}120^\circ\text{E}$, 55°N)
- 6) Dzhugdzhur, Stanovoy, Dzhagdy and Sikhote Alin Ranges ($\sim 120^\circ\text{-}140^\circ\text{E}$, $45^\circ\text{-}60^\circ\text{N}$)
- 7) Central and Koryak Ranges ($\sim 160^\circ\text{-}170^\circ\text{E}$, $\sim 55^\circ\text{-}60^\circ\text{N}$)
- 8) Brooks Range and MacKenzie Mountains ($\sim 200\text{-}230^\circ\text{E}$, $65^\circ\text{-}70^\circ\text{N}$)
- 9) Colorado Rockies ($\sim 250^\circ\text{E}$, 40°N)
- 10) The Laurentides and/or Notre Dame Mountains ($\sim 290^\circ\text{E}$, 50°N)
- 11) Iceland ($\sim 340^\circ\text{E}$, 65°N)
- 12) Northern Scotland ($\sim 355^\circ\text{E}$, 55°N)

Figure 15 plots time series of $\overline{\hat{T}_{ND}^2}(p)$ at 5 hPa over our four mountainous focus regions. In agreement with Figures 3b and 3e, a strong annual cycle is simulated at all 4 regions: indeed, essentially no MLS ND-viewable MWFm activity occurs outside of the winter season. There are hints that some of the site-to-site and interannual variability evident in the data is also reproduced, though the sparse data makes statistical attribution here inconclusive. In total, however, Figure 15 again supports a mountain wave interpretation for the winter variance enhancements evident in Figure 3.

[Insert Figure 15 here]

5.3 MWFM Results with MLS NA Filtering

As has been noted earlier, NA MLS views are less suited to observing mountain waves during winter. To assess this more quantitatively, we performed MWFM simulations like those in Figure 14b, but applied an MLS north-ascending (NA) filter (22) to the modeled mountain rays. Figure 16b plots $\overline{\hat{T}_{NA}^2}(p)$ at 5hPa, the NA analogue of $\overline{\hat{T}_{ND}^2}(p)$ in Figure 14b.

[Insert Figure 16 here]

We see that the vast majority of MWFM-simulated mountain wave activity is substantially suppressed or even removed compared to the ND map in Figure 14b, consistent with the MLS data (Figures 1a, 1c and 4) and our concept that NA views are less favorable for observing mountain waves during northern winter. However, what little activity remains in Figure 16b shows impressive agreement with the NA variances $(\tilde{\sigma}_A^2)_{NA}$ in Figure 16a. In particular, we see variance enhancements over southern and eastern Greenland, Iceland, the northern Urals, and Putoran Mountains in both model and data. We even see an enhancement over the northern Verkhoyansk Range (130°E, 65°-70°N) in northwestern Russia that occurs in both MWFM and MLS NA variance maps, but was not seen in the corresponding ND variances in Figure 14. The absences are just as significant too: for example, essentially no significant $(\tilde{\sigma}_A^2)_{NA}$ activity occurs over North America, as simulated in the corresponding MWFM $\overline{\hat{T}_{NA}^2}(p)$ map.

While the agreement between model and data in Figure 16 is not perfect in every respect, it is far better in comparison to the unfiltered MWFM mountain wave

climatology $\overline{\hat{T}^2}(p)$ in Figure 13, which bears little resemblance to the $(\tilde{\sigma}_A^2)_{NA}$ data.

Figure 16 leads us to the surprising conclusion that many of the high-latitude NA variance enhancements in Figures 1c/16a are in all likelihood mountain-wave-related.

The tendency for these NA mountain wave signals to cluster at high latitudes is due to the almost northward MLS views here at the top of the orbit, where both ND and NA views should have roughly similar sensitivity to waves propagating east-west (see Figures 7, 8 and 11). *Jiang et al.* [2003a] noted a similar effect during south yaw cycles when top-of-the-orbit observations viewed variance enhancements near the Rockies with near-southward MLS viewing. In addition, the well-known variability of the winter vortex flow [e.g., *Pawson and Naujokat*, 1999; *Waugh and Rong*, 2002] can potentially support stratospheric mountain waves with varying orientations with respect to this varying flow, sometimes yielding mountain waves with phase orientations more favorable to an NA view than in more typical undisturbed eastward flow regimes.

6. Discussion and Summary

The MLS instrument on UARS remains arguably our most important source of global data on gravity waves in the middle atmosphere, through the GW-related signals contained in its along-track limb radiances. With a next-generation MLS due for launch on the Earth Observing Satellite (EOS-Aura) platform in 2004 [*Waters et al.*, 1999], data from these two instruments offer the promise of an invaluable long-term database on GWs. Therefore it is very important that we develop a thorough understanding of the GW content of MLS radiance data, to provide a framework and context for analysis and interpretation of newer data to come.

A puzzling issue in MLS GW studies has been the lack of success in finding mountain wave signals in MLS data in the Northern Hemisphere. This work largely resolves the paradox. Combining careful MLS data analysis with global mountain wave “hindcast” modeling with the MWFM, we have concluded that there is a considerable amount of mountain wave information buried deep within MLS limb-track radiances at middle and high northern latitudes, on both ND and NA orbits.

The critical factor in our work was a detailed specification of how a spectrum of mountain waves with different 3D wavenumbers manifests as along-track radiance perturbations as the MLS instrument acquires limb radiances along its orbital track. This work built upon important initial work on this problem by *Wu and Waters* [1997] and *McLandress et al.* [2000]. Our so-called “MLS GW visibility function” was derived, tested and then implemented as a general module within the MWFM to simulate and interpret MLS MW measurements. Without this conduit between model and data, comparisons between MWFM predictions (Figure 13) and observations (Figures 1a and 1c) were mediocre at best, with large areas of ambiguity. These areas of discrepancy essentially reproduce the difficulties that earlier studies encountered in trying to associate structure in maps of MLS radiance variances from the northern winter stratosphere with mountain waves [e.g., *McLandress et al.*, 2000; *Jiang and Wu*, 2001]. On application of MLS GW visibility functions, much more conclusive comparisons between model and data arose, for both ND and NA orbit measurements (Figures 14 and 16).

Indeed, our model-data comparisons led us to associate a number of variance enhancements in MLS data with mountain waves generated by flow over variety of mountain ranges in the Northern Hemisphere. Three of our four focus regions (Scandinavia, southern Greenland, central Eurasia) showed properties entirely consistent

with stratospheric mountain wave enhancements. Indeed, mountain waves over southeastern Greenland appeared in both ND and NA views in both data and model variance maps. The fourth site (Queen Elizabeth Islands) also showed variance enhancements consistent with mountain waves, but modeled activity here was less geographically extensive than observed. MLS variance maps showed enhancements over a number of other mountain ranges that appeared to be mountain wave-induced also, as discussed and listed in sections 5.2 and 5.3.

The progress we have made here raises the question: can MLS data now be used to refine and constrain global mountain wave models and parameterization schemes, like the MWFM? At present, the answer to this is “possibly.” Since the MLS GW visibility function is so critical to attaining good model-data comparisons, any of its uncertainties in it translate into ambiguities in model-data comparisons, and hence in model validation. The current MLS GW visibility function is an analytical approximation specific to the limb-track data. Further numerical studies of MLS GW filtering and extensions to limb-scan data may be needed, for both MLS UARS and the new upcoming MLS on EOS-Aura. Because of these uncertainties, specific regions where model-data comparisons are poor cannot at present be unambiguously attributed to shortcomings in the model. Further work may reduce these uncertainties. For example, detailed site studies (e.g., at our focus regions) that locate and analyze large wave events may be helpful, to assess whether detailed models with MLS visibility effects included can reproduce the observations [see, e.g., the CRISTA case study of *Preusse et al.*, 2002].

Currently, though, discrepancies between model and data in Figures 14 and 16 may reflect several things. First, as just discussed, they may reflect shortcomings in our current specification of MLS GW visibility effects. Second, they may reflect episodic

noise or errors in MLS data. We believe, given the extensive averaging and quality control on MLS variances, that error/noise contamination effects are uncommon. Third, they may highlight shortcomings in the model output, both in the MWFM's basic physics and/or in the analyzed wind and temperature fields used to perform the hindcasts. Such defects are likely, and MLS data offer an attractive global data source to improve and validate the model. One current example worth studying might be the Queen Elizabeth Islands, where MWFM mountain wave activity is less extensive than observed variance enhancements (see Figure 14), which seem to be mountain wave-like.

A fourth possibility, though, is that model-data differences here indicate variance enhancements due to GWs from nonorographic sources, such as convective storms, unbalanced jet streams and fronts [e.g., *Fritts and Nastrom*, 1992]. For example, the NA variance enhancement over the Pacific in Figure 16a clearly cannot be mountain wave-induced. Over land, ND variance enhancements in Figure 14a arise in a zone $\sim 30^{\circ}$ - 60° E, 50° - 55° N over fairly flat regions of western Russia to the southernmost Urals in the east. While some of the easternmost activity here may be mountain waves associated with flow over the southern Urals, close correlations with MWFM data in Figure 14b are not evident. Substantial winter storms were documented during the early 1990s near the southern Ural mountains (*Lässig and Močalov*, 2000), as well as during February 1993 and December 1995 (*Lässig*, personal communication), which both fall within the MLS limb-scan and limb-track dates. Severe storms can be a strong source of gravity waves [e.g., *Fritts and Alexander*, 2003] and could potentially explain some of the observed variance structure here. Further analysis is needed to assess these and other speculations.

The next generation MLS on EOS-Aura significantly improves the vertical resolution over UARS MLS. The 118GHz radiometer has a *6.5 km* vertical and *13 km* horizontal

field of view, which should be able to resolve GWs with vertical wavelengths of ~ 4 km and across-track horizontal wavelengths down to ~ 200 km. Our analysis here suggests that data from this instrument should contribute significant observations on mountain waves in the extratropical winter northern stratosphere.

Acknowledgements

We thank James Holton and Ted Shepherd, as well as our colleagues in the MLS Atmospheric Science Team for encouragement and suggestions during the development of this study. This work was supported by the National Aeronautics and Space Administration (NASA) ACPMAP program (grants ACPMAP-0000-0072 and W19946) and Geospace Sciences program (grant W19862). The authors also acknowledge support from the Jet Propulsion Laboratory, California Institute of Technology, under contract with NASA, and the Office of Naval Research through the NRL 6.1 and 6.2 research programs

Jonathan H. Jiang and Dong L. Wu, Jet Propulsion Laboratory, California Institute of Technology,
Mail-Stop 183-701, 4800 Oak Grove Drive, Pasadena, California 91109-8099, U.S.A. E-mails:
jonathan@mls.jpl.nasa.gov; dwu@mls.jpl.nasa.gov.

Stephen D. Eckermann, Middle Atmosphere Dynamics Section, Code 7646, Naval Research Laboratory,
Washington, DC 20375. E-mail: stephen.eckermann@nrl.navy.mil.

Jun Ma, Computational Physics, Inc., Springfield, Virginia 22151, USA. Email: junma@uap2.nrl.navy.mil.

References

- Alexander, M. J., Interpretations of observed climatological patterns in stratospheric gravity wave variance, *J. Geophys. Res.*, *103*, 8627-8640, 1998.
- Andrews, D. G., The influence of atmospheric waves on the general circulation of the middle atmosphere, *Phil. Trans. R. Soc. Lond., Ser. A*, *323*, 693-705, 1987.
- Anton, H., Elementary Linear Algebra, 8th Edition, Wiley, 2000.
- Bacmeister, J. T., Mountain-wave drag in the stratosphere and mesosphere inferred from observed winds and a simple mountain-wave parameterization scheme, *J. Atmos. Sci.*, *50*, 377-399, 1993.
- Bacmeister, J. T., P. A. Newman, B. L. Gary, and K. R. Chan, An algorithm for forecasting mountain wave related turbulence in the stratosphere, *Wea. Forecasting*, *9*, 241-253, 1994.
- Bacmeister, J. T., S. D. Eckermann, A. Tsias, K. S. Carslaw, and T. Peter, Mesoscale temperature fluctuations induced by a spectrum of gravity waves: A comparison of parameterizations and their impact on stratospheric microphysics, *J. Atmos. Sci.*, *56*, 1913-1924, 1999.
- Broutman, D., J. W. Rottman and S. D. Eckermann, A hybrid method for analyzing wave propagation from a localized source, with application to mountain waves, *Q. J. R. Meteorol. Soc.*, *127*, 129-146, 2001.
- Carslaw, K. S., M. Wirth, A. Tsias, B. P. Luo, A. Dörnbrack, M. Leutbecher, H. Volkert, W. Renger, J. T. Bacmeister, E. Reimer, and T. Peter, Increased stratospheric ozone depletion due to mountain-induced atmospheric waves, *Nature*, *391*, 675-678, 1998.
- Cusack, S., J. M. Edwards, and R. Kershaw, Estimating the subgrid variance of saturation, and its parameterization for use in a GCM cloud scheme, *Q. J. R. Meteorol. Soc.*, *125*, 3057-3076, 1999.
- Dörnbrack, A., and M. Leutbecher, Relevance of mountain waves for the formation of polar stratospheric clouds over Scandinavia: A 20 year climatology, *J. Geophys. Res.*, *106*, 1583-1593, 2001.
- Dörnbrack, A., T. Birner, A. Fix, H. Fientje, A. Meister, H. Schmid, E. V. Browell, and M. J. Mahoney, Evidence for inertia gravity waves forming polar stratospheric clouds over Scandinavia, *J. Geophys. Res.*, *107(D20)*, 8287, doi:10.1029/2001JD000452, 2002.
- Duck, T. J., and J. A. Whiteway, Seasonal transition in gravity wave activity during the springtime stratospheric vortex breakdown, *Geophys. Res. Lett.*, *27*, 3477-3480, 2000.

- Duck, T. J., J. A. Whiteway, and A. I. Carswell, Lidar observations of gravity wave activity and Arctic stratospheric vortex core warming, *Geophys. Res. Lett.*, **25**, 2813-2816, 1998.
- Eckermann, S. D., Ray-tracing simulation of the global propagation of inertia gravity waves through the zonally-averaged middle atmosphere, *J. Geophys. Res.*, **97**, 15,849-15,866, 1992.
- Eckermann, S. D., On the observed morphology of gravity-wave and equatorial-wave variance in the stratosphere, *J. Atmos. Terr. Phys.*, **57**, 105-134, 1995 (corrigendum *J. Atmos. Terr. Phys.*, **57**(6), I, 1995).
- Eckermann, S. D., and P. Preusse, Global measurements of stratospheric mountain waves from space, *Science*, **286**, 1534-1537, 1999.
- Eckermann, S. D., I. Hirota, and W. K. Hocking, Gravity-wave and equatorial-wave morphology of the stratosphere derived from long-term rocket soundings, *Quart. J. Roy. Meteor. Soc.*, **121**, 149-186, 1995.
- Fritts, D. C., and M. J. Alexander, Gravity wave dynamics and effects in the middle atmosphere, *Rev. Geophys.* **41**(1), 1003, doi:10.1029/2001RG000106, 2003.
- Fritts, D. C., and G. D. Nastrom, Sources of mesoscale variability of gravity waves, II, frontal, convective, and jet stream excitation, *J. Atmos. Sci.*, **49**, 111-127, 1992.
- Fritts, D. C., and T. E. VanZandt, Spectral estimates of gravity wave energy and momentum fluxes, I, energy dissipation, acceleration, and constraints, *J. Atmos. Sci.*, **50**, 3685-3694, 1993.
- Gjevik, B., and T. Marthinsen, Three-dimensional lee-wave pattern, *Q. J. R. Meteorol. Soc.*, **104**, 947-957, 1978.
- Hamilton, K., Comprehensive meteorological modeling of the middle atmosphere: A tutorial review, *J. Atmos. Terr. Phys.*, **58**, 1591-1627, 1996.
- Hertzog, A., F. Vial, A. Dörnbrack, S. D. Eckermann, B. M. Knudsen, and J.-P. Pommereau, In-situ observations of gravity waves and comparisons with numerical simulations during the SOLVE/THESEO 2000 campaign, *J. Geophys. Res.*, **107**(D20), 8292, doi:10.1029/2001JD001025, , 2002.
- Hirota, I., and T. Niki, A statistical study of inertia-gravity waves in the middle atmosphere. *J. Meteor. Soc. Japan*, **63**, 1055-1066, 1985.
- Holton, J. R., and M. J. Alexander, The role of waves in the transport circulation of the middle atmosphere, in *Atmospheric Science Across the Stratopause*, D. E. Siskind, S. D. Eckermann and M. E. Summers eds., AGU Geophysical Monograph Series, **123**, 21-35, 2000.

- Jarnot, R. F., R. E. Cofield, J. W. Waters, D. A. Flower, and D. E. Peckham, Calibration of the Microwave Limb Sounder on the Upper Atmosphere Research Satellite, *J. Geophys. Res.*, *101*, 9957-9982, 1996.
- Jensen, E. J. and O. B. Toon, Ice nucleation in the upper troposphere - sensitivity to aerosol number density, temperature, and cooling rate, *Geophys. Res. Lett.*, *21*, 2019-2022, 1994.
- Jiang, J. H., and D. L. Wu, UARS MLS observation of gravity waves associated with the Arctic winter stratospheric vortex, *Geophys. Res. Lett.*, *28*, 527-530, 2001.
- Jiang, J.H., D.L. Wu, S.D. Eckermann, Upper Atmosphere Research Satellite (UARS) MLS observation of mountain waves over the Andes, *J. Geophys. Res.* *107*(D20), 8273, doi:10.1029 /2002JD002091, 2002.
- Jiang, J. H., D. L. Wu, S. D. Eckermann, and J. Ma, Mountain waves in the middle atmosphere: Microwave Limb Sounder Observations and Analyses, *Adv. Space Res.*, (in press), 2003a.
- Jiang, J. H., B. Wang, K. Goya, K. Hocke, S. D. Eckermann, J. Ma, D. L. Wu, W. G. Read, and J. C. McConnell, Geographical Distribution and inter-seasonal variability of tropical deep-convection: UARS MLS observations and analyses, submitted to *J. Geophys. Res.*, 2003b.
- Kim, Y.-J., S. D. Eckermann, and H.-Y. Chun, An overview of the past, present and future of gravity-wave drag parametrization for numerical climate and weather prediction models, *Atmos. Ocean*, *41*, 65-98, 2003.
- Koch, S. E., and L. M. Siedlarz, Mesoscale gravity waves and their environment in the central United States during STORM-FEST, *Mon Weather Rev.*, *127*, 2854-2879, 1999.
- Lässig, R. and S. A. Močálov, Frequency and characteristics of severe storms in the Urals and their influence on the development, structure and management of the boreal forests, *Forest Ecology and Management*, *135*, 179-194, 2000.
- Lau, C. L., G. E. Peckham, R. A. Suttie, and R. F. Jarnot, Characterization of MLS 1/f noise parameters, *Int. J. Remote Sens.*, *17*, 3751-3759, 1996.
- Leutbecher, M., and H. Volkert, The propagation of mountain waves into the stratosphere: quantitative evaluation of three-dimensional simulations, *J. Atmos. Sci.*, *57*, 3090-3108, 2000.
- Marks, C. J., and S. D. Eckermann, A three-dimensional nonhydrostatic ray-tracing model for gravity waves: Formulation and preliminary results for the middle atmosphere, *J. Atmos. Sci.*, *52*, 1959-1984, 1995.

- McIntyre, M. E., Global effects of gravity waves in the middle atmosphere: A theoretical perspective, *Adv. Space Res.*, 27(10), 1723-1736, 2001.
- McLandress, C., On the importance of gravity waves in the middle atmosphere and their parameterization in general circulation models, *J. Atmos. Terr. Phys.*, 60, 1357-1383, 1998.
- McLandress, C., M. J. Alexander, and D. L. Wu, Microwave limb sounder observations of gravity waves in the stratosphere: a climatology and interpretation, *J. Geophys. Res.*, 105, 11947-11967, 2000.
- Nastrom, G. D. and Fritts, D. C., Sources of mesoscale variability of gravity waves, 1, topographic excitation, *J. Atmos. Sci.*, 49, 101-110, 1992.
- National Geographic Atlas of the World, 6th. edition (revised), 136 pp, National Geographic Society, Washington, DC, 1995.
- Pawson, S., and B. Naujokat, The cold winters of the middle 1990s in the northern lower stratosphere, *J. Geophys. Res.*, 104, 14,209-14,222, 1999.
- Pierce, R. B., J. Al-Saadi, T. D. Fairlie, M. Natarajan, V. L. Harvey, W. L. Grose, J. M. Russell, R. Bevilacqua, S. D. Eckermann, D. Fahey, P. Popp, E. Richard, R. Stimpfle, G. C. Toon, C. R. Webster, and J. Elkins, Large-scale chemical evolution of the Arctic vortex during the 1999-2000 winter: HALOE/POAM3 Lagrangian photochemical modeling for the SAGE III Ozone Loss and Validation (SOLVE) Campaign, *J. Geophys. Res.*, 108(D5), 8317, doi:10.1029/2001JD001063, 2003.
- Preusse, P., A. Dörnbrack, S. D. Eckermann, M. Piese, B. Schaefer, J. T. Bacmeister, D. Broutman, and K.U. Grossmann, Space based measurements of stratospheric mountain waves by CRISTA, 1, sensitivity, analysis method and a case study, *J. Geophys. Res.*, 107(D23), 8178, 10.1029/2001JD000699, , 2002.
- Swinbank, R., and A. O'Neill, A stratosphere-troposphere data assimilation system, *Mon. Wea. Rev.*, 122, 686-702, 1994.
- Thayer, J. P., M. Rapp, A. J. Gerrard, E. Gudmundsson, and T. J. Kane, Gravity-wave influences on Arctic mesospheric clouds as determined by a Rayleigh lidar at Sondrestrom, Greenland, *J. Geophys. Res.*, 108(D8), 8449, doi:10.1029/2002JD002363, 2003.
- Tsuda, T., M. Nishida, C. Rocken, and R.H. Ware, A global morphology of gravity wave activity in the stratosphere revealed by the GPS occultation data (GPS/MET), *J. Geophys. Res.*, 105, 7257-7273, 2000.
- Waters, J. W., W.G. Read, L. Froidevaux, R.F. Jarnot, R.E. Cofield, D.A. Flower, G.K. Lau, H.M. Pickett, M.L. Santee, D.L. Wu, M.A. Boyles, J.R. Burke, R.R. Lay, M.S. Loo, N.J. Livesey, T.A. Lungu, G.L. Manney, L.L. Nakamura, V.S. Perun,

- B.P. Ridenoure, Z. Shippony, P.H. Siegel, R.P. Thurstans, R.S. Harwood, H.C. Pumphrey, M.J. Filipiak, The UARS and EOS Microwave Limb Sounder (MLS) experiments, *J. Atmos. Sci.*, *56*, 194-218, 1999.
- Waugh, D. W., and P. P. Rong, Interannual variability in the decay of lower stratospheric Arctic vortices, *J. Meteorol. Soc. Japan*, *80*, 997-1012, 2002.
- Whiteway, J. A., Enhanced and inhibited gravity wave spectra, *J. Atmos. Sci.*, *56*, 1344-1352, 1999.
- Whiteway, J. A., and T. J. Duck, Evidence for critical level filtering of atmospheric gravity waves, *Geophys. Res. Lett.*, *23*, 145-148, 1996.
- Whiteway, J. A., and T. J. Duck, Enhanced Arctic stratospheric gravity wave activity above a tropospheric jet, *Geophys. Res. Lett.*, *26*, 2453-2456, 1999.
- Wu, D. L., Horizontal wavenumber spectrum of MLS radiances, *J. Atmos. Solar-Terr. Phys.* *63*, 1465-1477, 2001.
- Wu, D.L., and J.H. Jiang, MLS observation of atmospheric gravity waves over Antarctica, *J. Geophys. Res.*, *107*(D24), 4773, doi: 10.1029/2002JD002390, 2002.
- Wu, D. L., and J. W. Waters, Gravity-wave-scale temperature fluctuations seen by the UARS MLS, *Geophys. Res. Lett.*, *23*, 3289-3292, 1996a.
- Wu, D. L., and J. W. Waters, Satellite observations of atmospheric variances: A possible indication of gravity waves, *Geophys. Res. Lett.*, *23*, 3631-3634, 1996b.
- Wu, D. L., and J. W. Waters, Observations of Gravity Waves with the UARS Microwave Limb Sounder, *Gravity Wave Processes, NATO ASI Series I: Global Environmental Change*, *50*, 103-120, 1997.

Combined Channel (#)	Approximate Height (km)	Limb-track $\frac{\sigma_N^2}{2}$ (K²)	Limb-scan $\frac{\sigma_N^2}{2}$ (K²)	$\frac{(\text{Noise}_{\text{Wu97}})^2}{2}$
1/15	28	0.0018	0.0022	0.0025
2/14	33	0.0027	0.0034	0.0032
2/13	38	0.0048	0.0051	0.0072
4/12	43	0.0096	0.010	0.016
5	48	0.038	0.039	0.034
6/10	53	0.039	0.040	0.068
7/9	61	0.070	0.071	0.12
8	80	0.13	0.13	0.10

Table 1: Estimated MLS 63 GHz channel noises variances, for limb-track (3rd column) and limb-scan (4th column) variances, compared with the calibrated noise values from *Wu and Waters* [1997]. Note: most channel data are combined, except channels 5 and 11, to reduce the net noise variance (channel 11 did not function during the UARS MLS mission).

Figure 1: (a) Variances $\tilde{\sigma}_A^2$ from MLS channels 3/13 limb-track measurements ($z \sim 38$ km) during north-looking descending (ND) orbit segments in the Northern Hemisphere winter stratosphere. These data are averaged on a $10^\circ \times 4^\circ$ longitude-latitude grid during winter months (December through February) of 1994-1997. The dotted contour lines are UKMO assimilated mean stratospheric winds at pressure altitudes between ~ 6.8 -4.6 hPa, averaged on the same $10^\circ \times 4^\circ$ longitude-latitude grid during the same MLS limb-track days, and interpolated onto the same limb-track orbits. The color bar scale for radiance variance is linear. (b) Digital elevations of northern hemispheric land masses, plotted using the “ETOPO5” 5-minute gridded digital elevation model issued by the National Geophysical Data Center. Locations and names of mountain ranges were derived from various sources, the main being National Geographic Atlas of the World (1995). The elevation color bar scale is linear. (c) as for (a), but plotting variances on north-looking ascending orbits (NA).

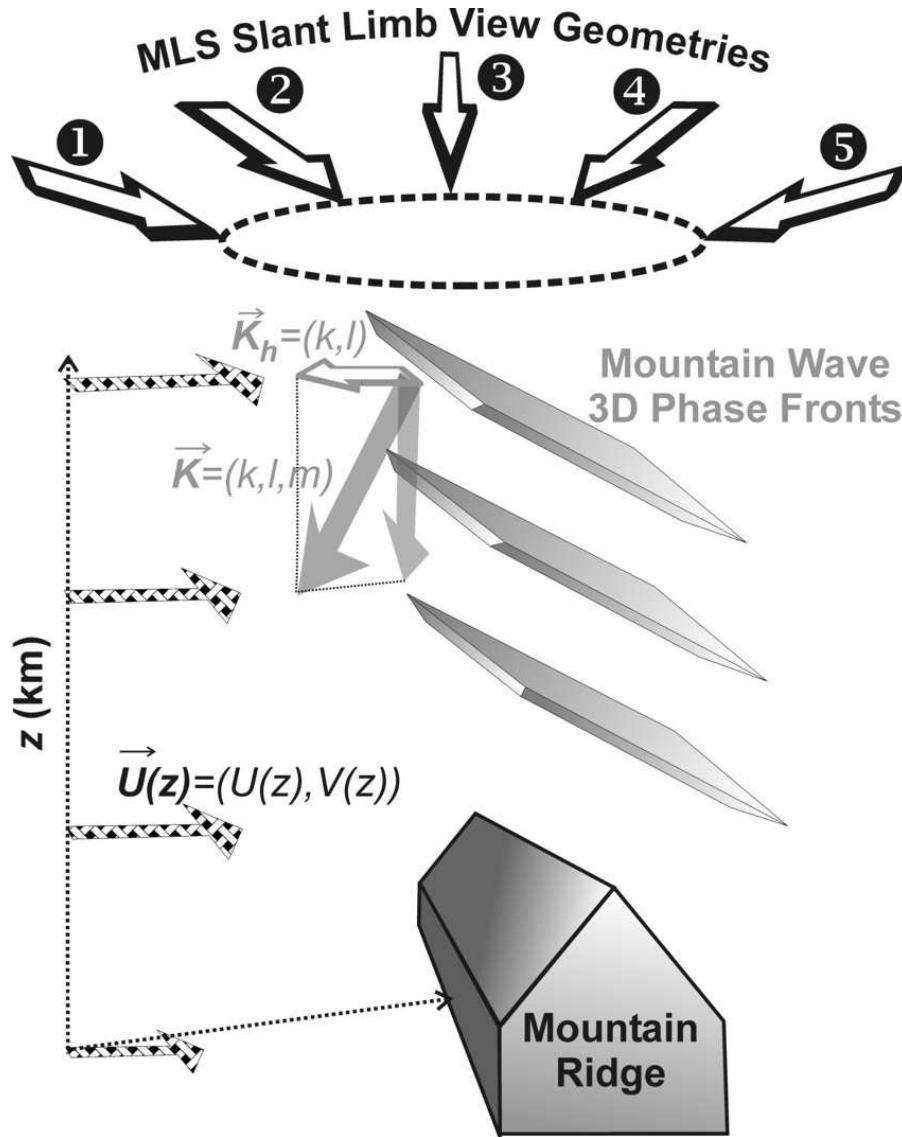
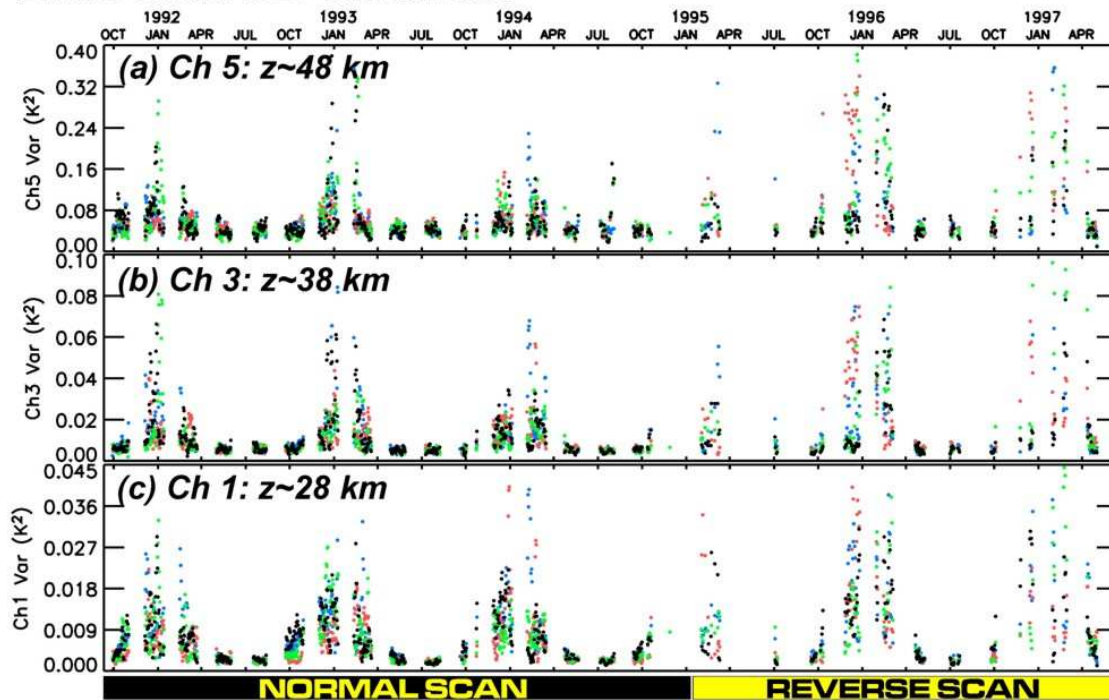


Figure 2: Schematic 3D depiction of mountain waves forced by horizontal flow (U, V) over an idealized mountain ridge. The wind profile (depicted with hatched vectors) remains largely eastward through the stratosphere ($U > 0$), supporting stratospheric mountain waves with horizontal wavenumbers directed westward ($k < 0$) with three-dimensional phase fronts oriented broadly as depicted. Five potential MLS slant viewing geometries, spanning 180° in azimuth and labeled 1 through 5, are shown above this mountain wave and are envisaged as passing through its three-dimensional structure while acquiring saturated radiances from this volume of atmosphere directly above the ridge. Viewing geometry 2 is most favorable for resolving this wave perturbation in saturated along-track radiances, since it views quasi-parallel to the wave's phase fronts and projects a long horizontal wavelength along the LOS, yielding less along-path smearing of the wave oscillation. Conversely, view 5 views the limb across the wave's phase fronts and so will tend to smear out the wave in each instantaneous limb radiance measurement.

Figure 2

Limb Scan ND Variances



Limb Track ND Variances

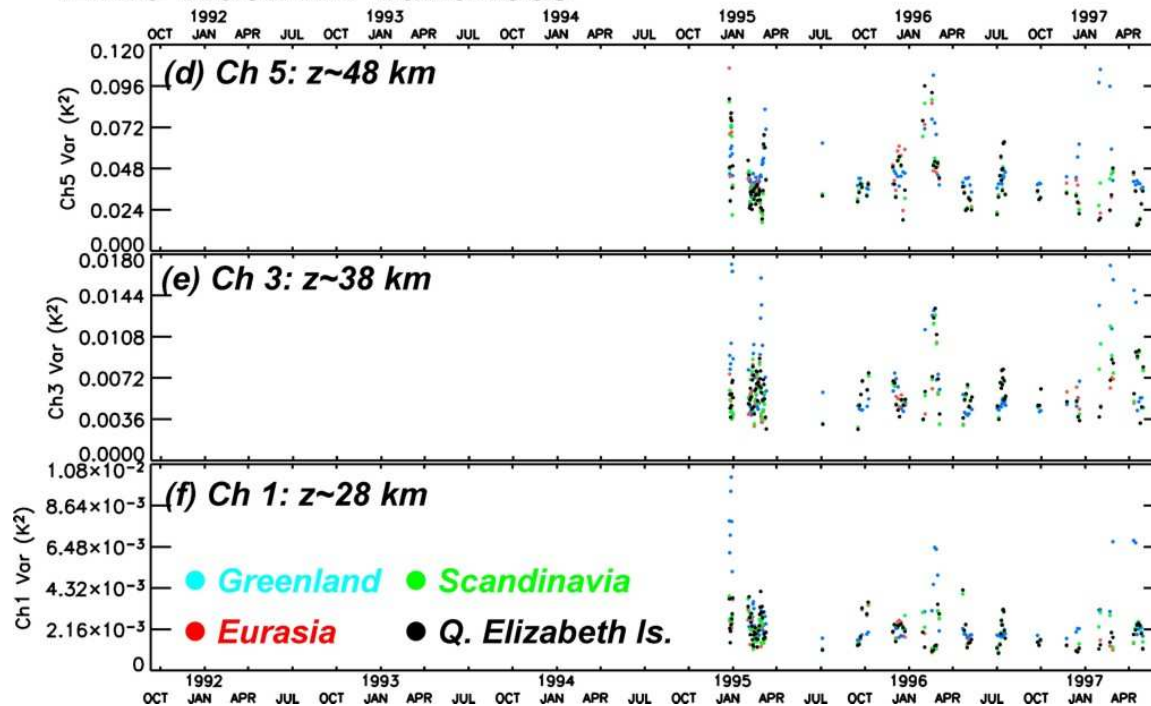


Figure 3

Figure 3: Time-series of daily-mean MLS limb-scan GW variances (panels *a-c*) for normal-scan period (October 1991 to December 1994), reverse-scan period (January 1995 to May 1997), and daily-mean MLS limb-track GW variances (panels *d-f*) from December 1994 to May 1997. The variances are from UARS MLS north-looking descending orbits at three different altitudes of 28 km (channels 1/15), 38 km (channels 3/13), and 48 km (channels 5) over four selected focus regions: southern Greenland (55°N-70°N; 20°-60°W; blue); central Eurasia (45°N-65°N; 80°-130°E; red), Scandinavia (55°N-70°N; 5°-40°E; green); Queen Elizabeth Islands (65°N-75°N; 80°-120°W; black). A 3-day running mean was applied to the daily averages to smooth-out the large fluctuations in the daily variances.

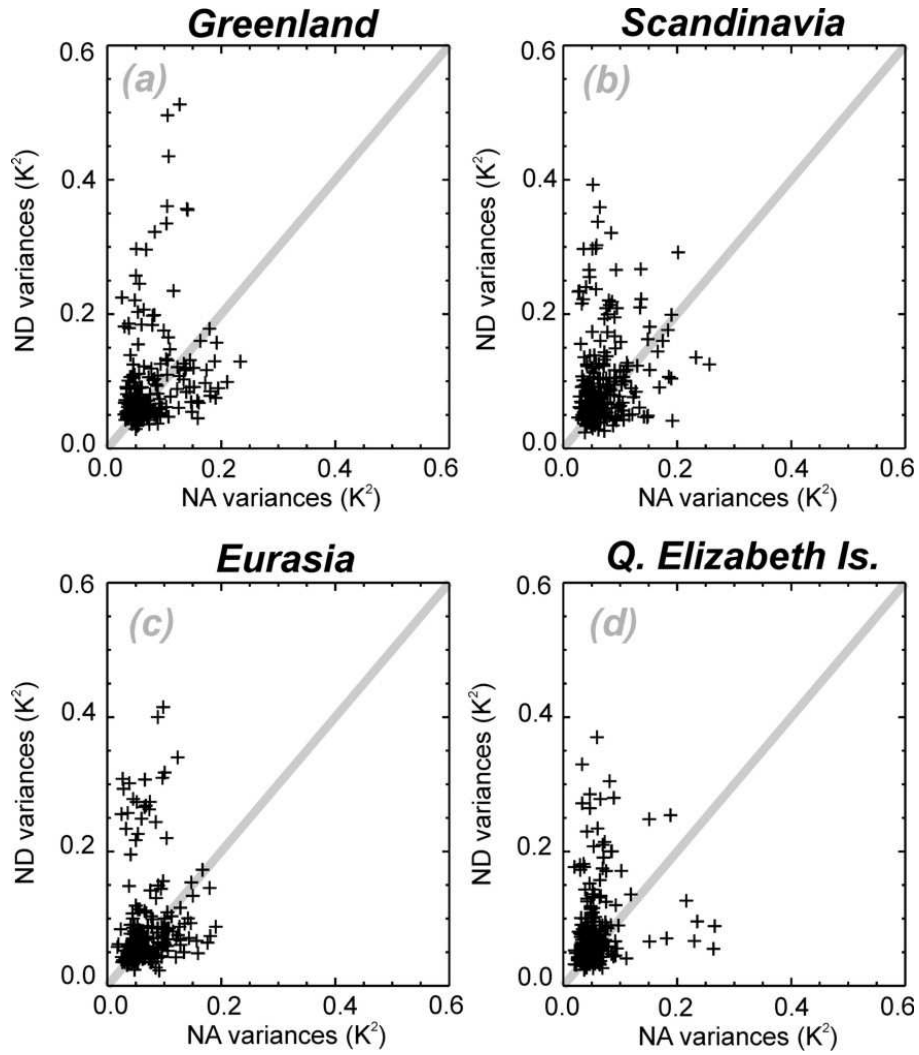


Figure 4: Scatter-plot of daily-mean variances at the four focus regions, derived from limb-scan radiance measurements (1991-97) from channels 3 and 13 ($z \sim 38$ km) on north-looking descending (ND) and ascending (NA) orbits for winter months (December-February). The variances are computed in the same way and for the same four regions as in Figure 3.

Figure 4

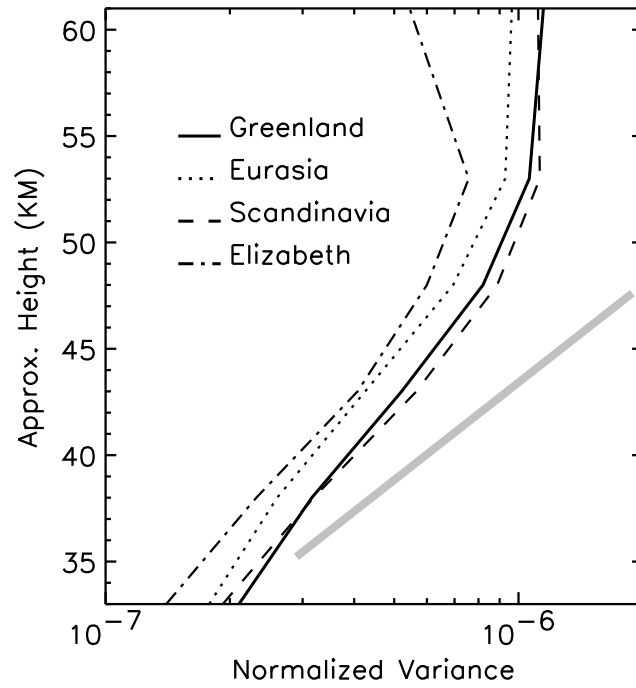


Figure 5: Vertical growth of variances over southern Greenland, central Eurasia, Scandinavia, and Queen Elizabeth Islands for Arctic winters (1991-97) as observed in limb scans by MLS on north-looking descending (ND) orbits. The variances are normalized by the mean-square radiance brightness temperature. Instrument noise was removed from these variances. The grey curve shows sample $\exp\left(\int dz / H_\rho\right)$ growth with $H_\rho = 7$ km.

Figure 5

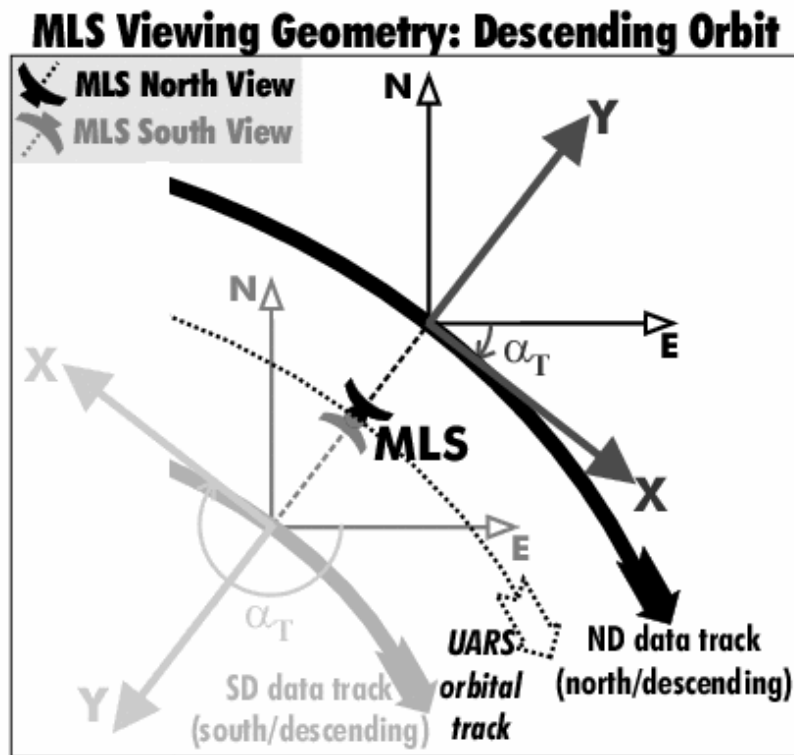


Figure 6: Schematic diagram of the in-orbit geometry of the MLS observation for a north/descending (ND) orbit segment. See text for additional details

Figure 6

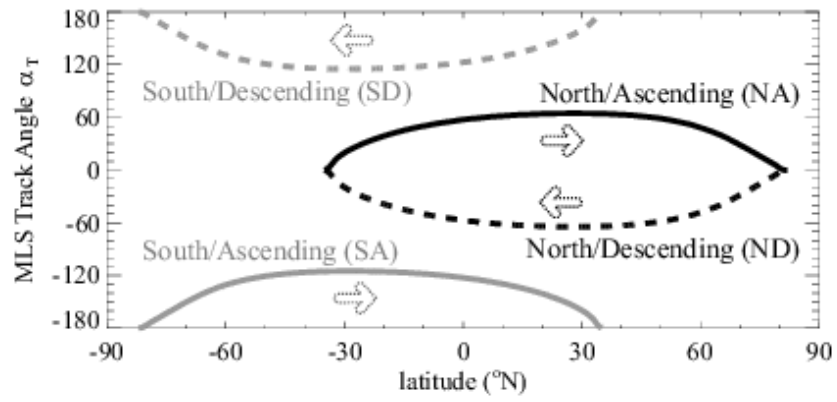


Figure 7: Track angles α_T as a function of latitude for both ascending (solid lines) and descending orbits (dashed lines). North and south viewing orbital geometries are shown with black and grey curves, respectively. The satellite motion along each orbit segment is arrowed.

Figure 7

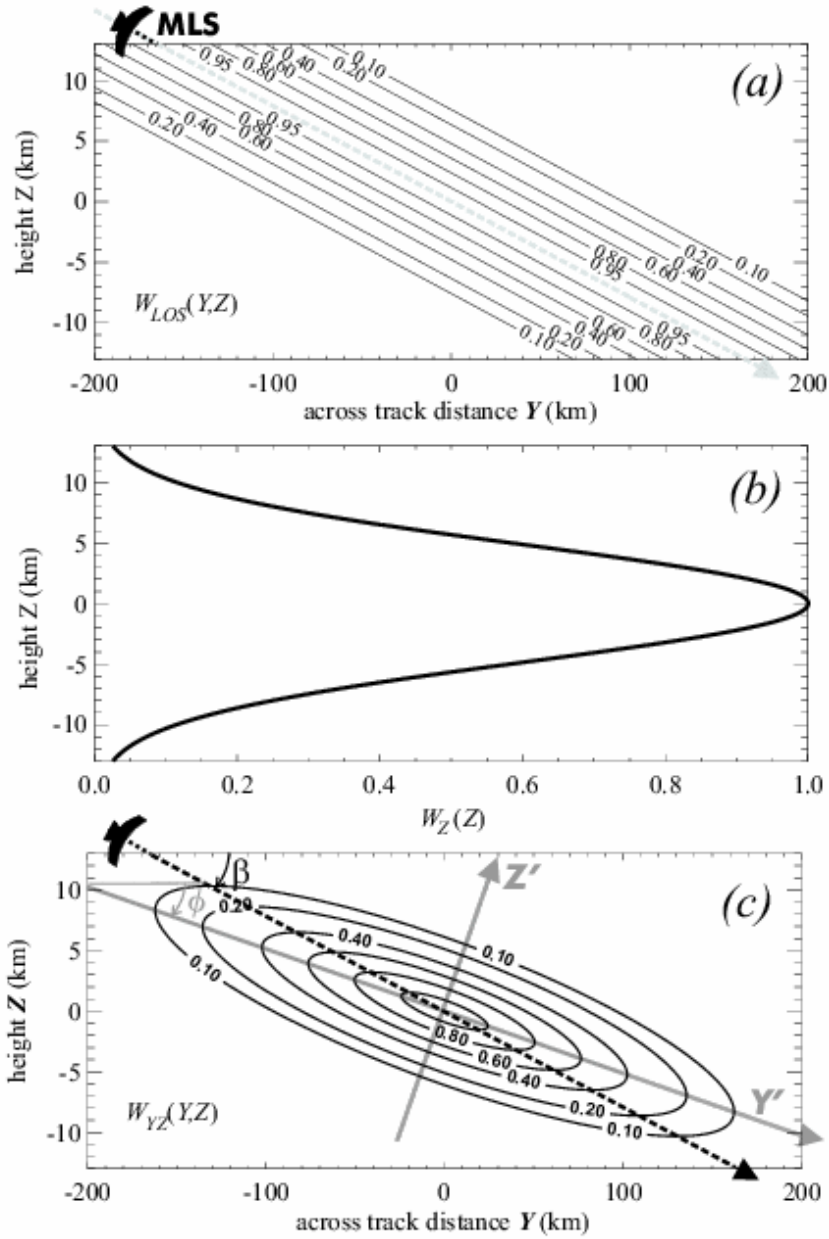


Figure 8: a) MLS LOS at an angle β below the horizontal and the symmetric response around this LOS due to the antenna width; b) Gaussian fit to the vertical temperature weighting function for MLS channels 3 and 13; c) the net 2-D MLS weighting function $W_{YZ}(Y, Z)$.

Figure 8

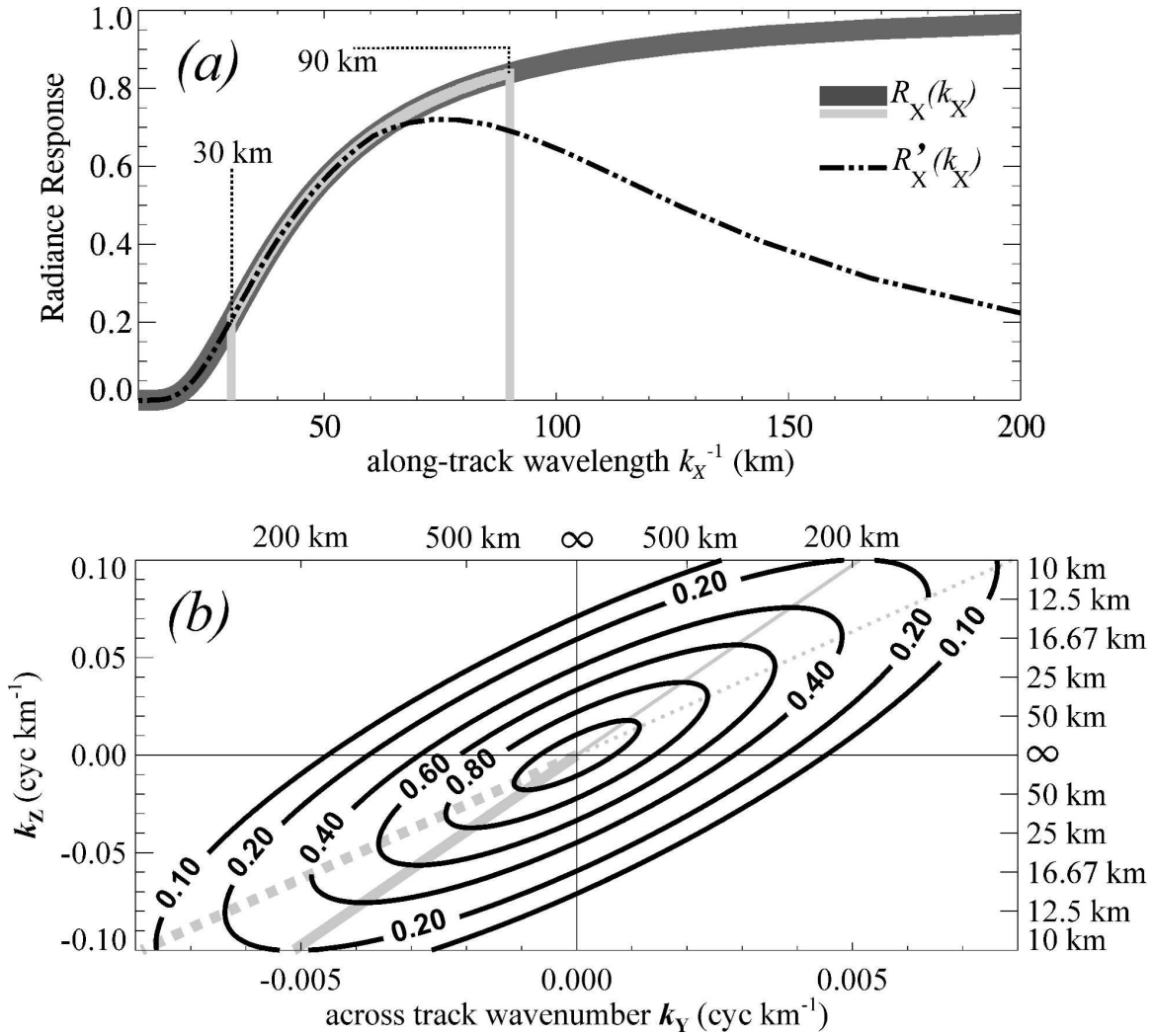


Figure 9: a) MLS along-track visibility $R_X(k_X)$ (solid dark curve) and the band-pass portion between cutoff wavelengths of 30 km and 90 km (light solid curve). Black broken curve shows the modified along-track visibility $R'_X(k_X)$ from (21); b) 2-D MLS spectral visibility function $R_{Y'}(k_{Y'})R_{Z'}(k_{Z'})$. Grey lines are explained in the text.

Figure 9

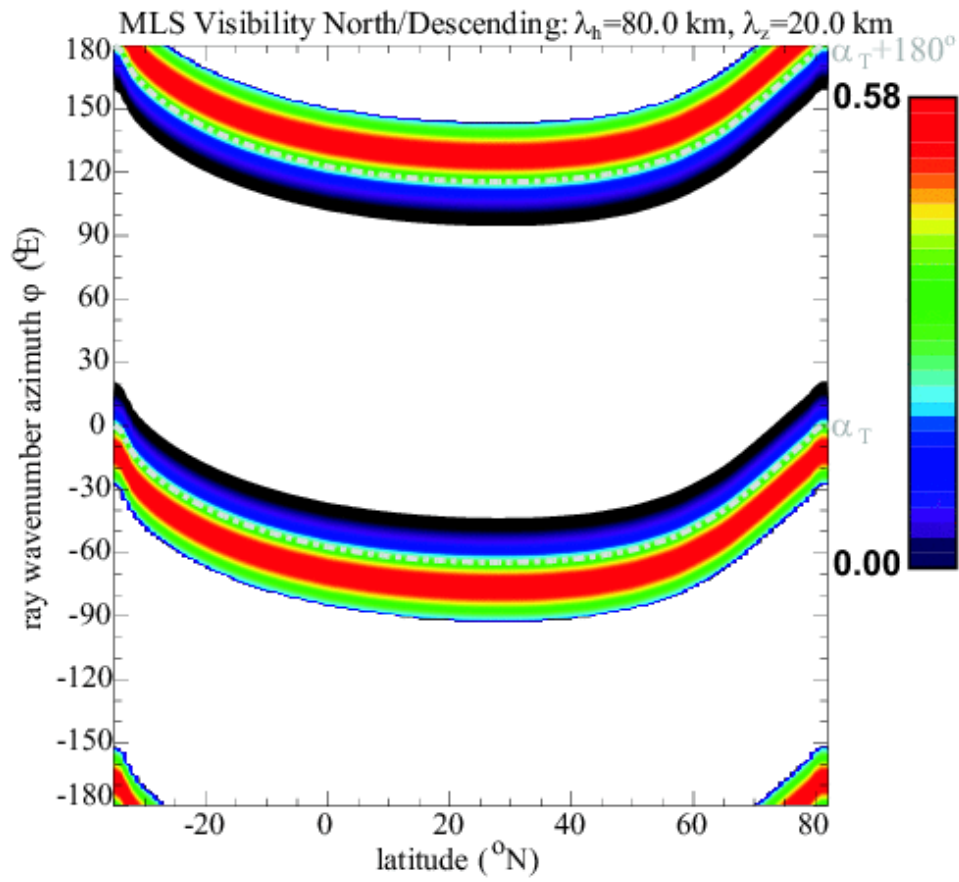


Figure 10: MLS visibility for GWs with 80km horizontal and 20km vertical wavelengths as a function of latitude and wave propagation azimuth for north-looking descending (ND) orbits. Color bar scale is linear.

Figure 10

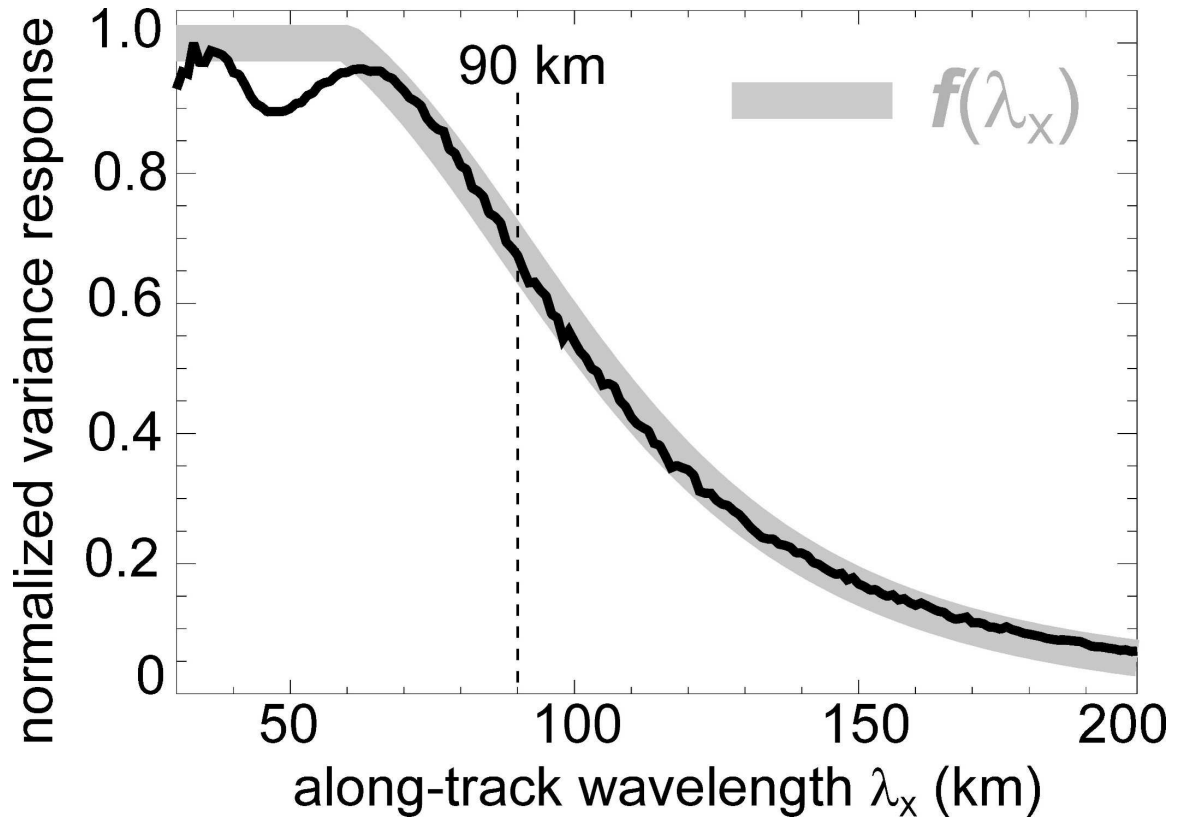


Figure 11: Black curve shows mean normalized variance response of a gravity wave of given along-track wavelength λ_x extracted using the 6-point variance calculation (1). Each point is the mean of 1000 computations using a randomly phase gravity wave. Grey curve is the analytical functional fit $f(\lambda_x)$ given by (20).

Figure 11

**MLS “Polar Diagram” of Visibility
to Gravity Waves of Given \vec{K}**

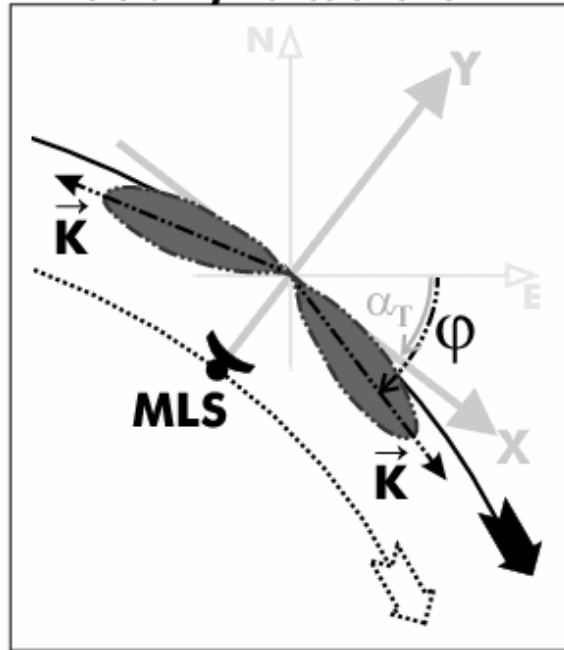


Figure 12: Schematic “polar diagram” of MLS 6-point limb-tracking visibility to a GW of a given wavenumber \vec{K} directed at various azimuths φ .

Figure 12

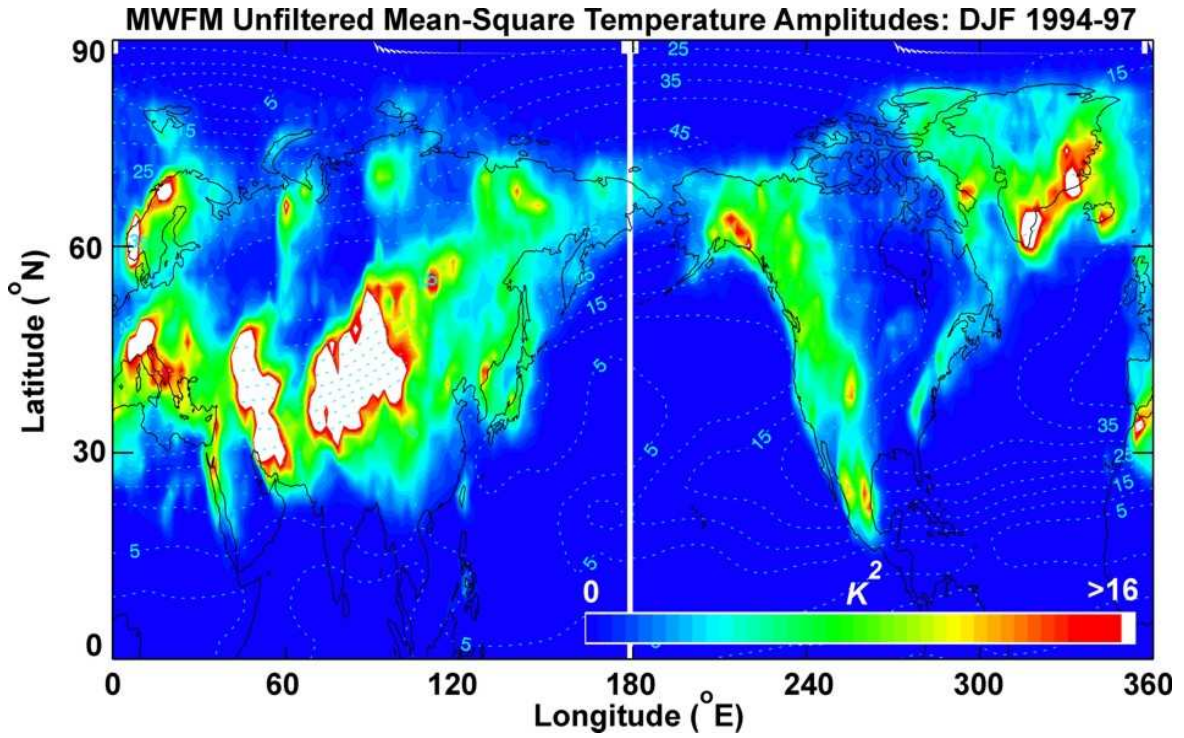


Figure 13: MWFM-simulated $\overline{\hat{T}^2}(p)$, the mountain wave mean-square peak temperature amplitudes (K^2) at 5 hPa ($z \sim 37$ km) without any observational filtering applied. Results are averaged in $10^\circ \times 4^\circ$ grid boxes for winter (December-January-February), years 1994-1997, and are averaged for selected MLS limb-track days. The dotted contour lines are UKMO assimilated total stratospheric winds ($m s^{-1}$) for this level averaged on the same longitude-latitude grids for the same MLS limb-track days. The color bar scale is linear.

Figure 13

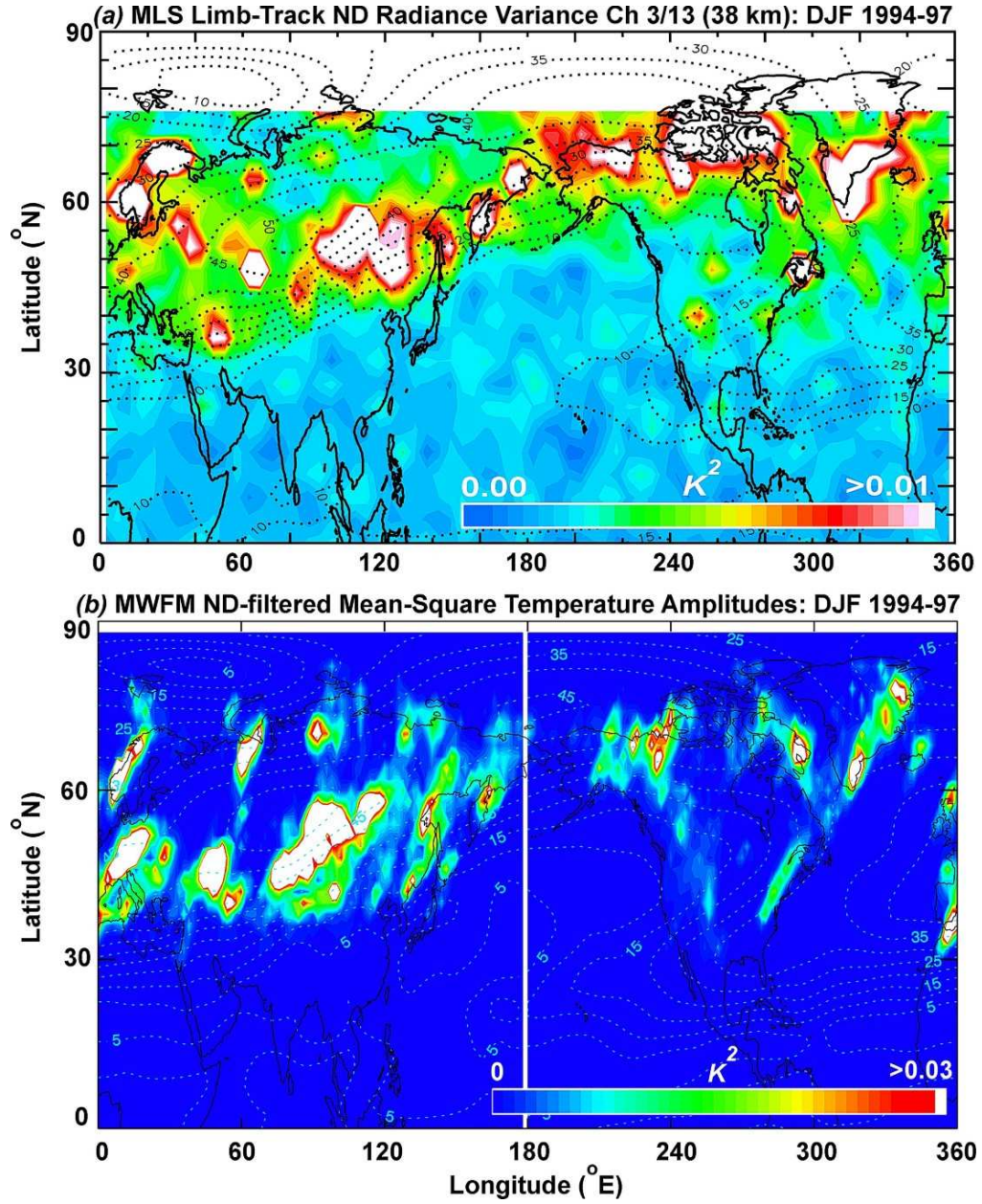


Figure 14: (a) MLS ND limb-track radiance variances $\tilde{\sigma}_A^2$ from channels 3/13 ($z \sim 38$ km), from Figure 1a. (b) $\hat{T}_{ND}^2(p)$, the gridbox-averaged MWFM mean-square peak mountain wave temperature amplitudes at 5 hPa ($z \sim 37$ km) after application of the MLS ND GW visibility filter (22). Data in both maps have been averaged on a $10^\circ \times 4^\circ$ longitude-latitude grid during winter months (December-February) of 1994-1997. Dotted contour are UKMO assimilated mean total stratospheric winds ($m s^{-1}$) at the indicated level during limb-track days. Both color bar scales are linear: while both color bar scales have similar ranges, $(\tilde{\sigma}_A^2)_{ND}$ and $\hat{T}^2(p)$, though related, are essentially different and so the similarity of their absolute values is largely serendipitous. For example, different choices of I_K and I_ϕ in would have changed the absolute values of $\hat{T}^2(p)$. Relative differences in each case, however, are comparable and hence significant.

Figure 14

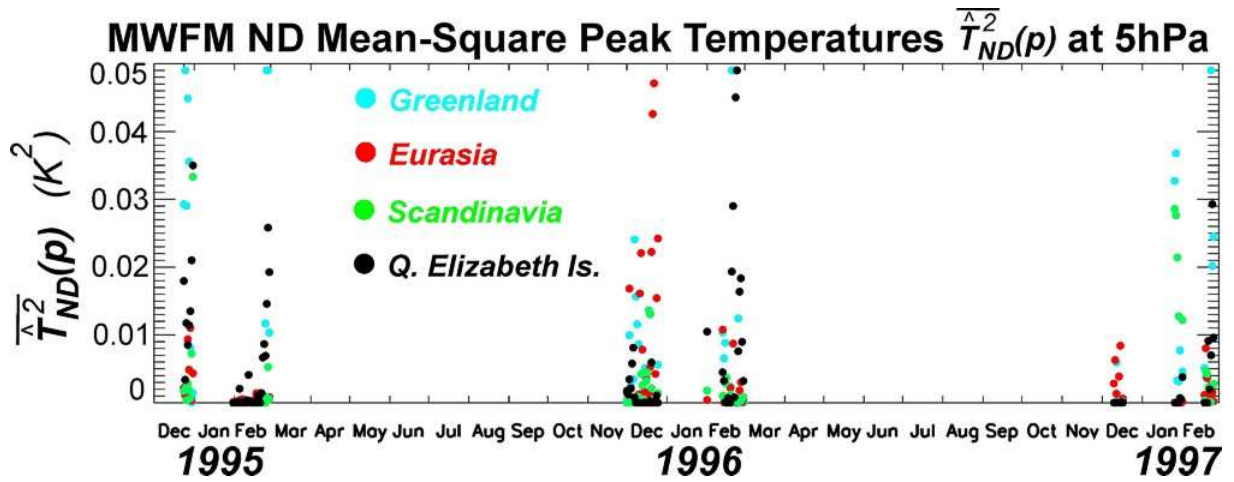


Figure 15: Time series of MWFM-simulated mean-square peak mountain wave temperature amplitudes, $\hat{T}_{ND}^2(p)$ at 5 hPa ($z \sim 37$ km) over southern Greenland (blue), central Eurasia (red), Scandinavia (green) and the Queen Elizabeth Islands (black) for the period of MLS limb-track measurements.

Figure 15

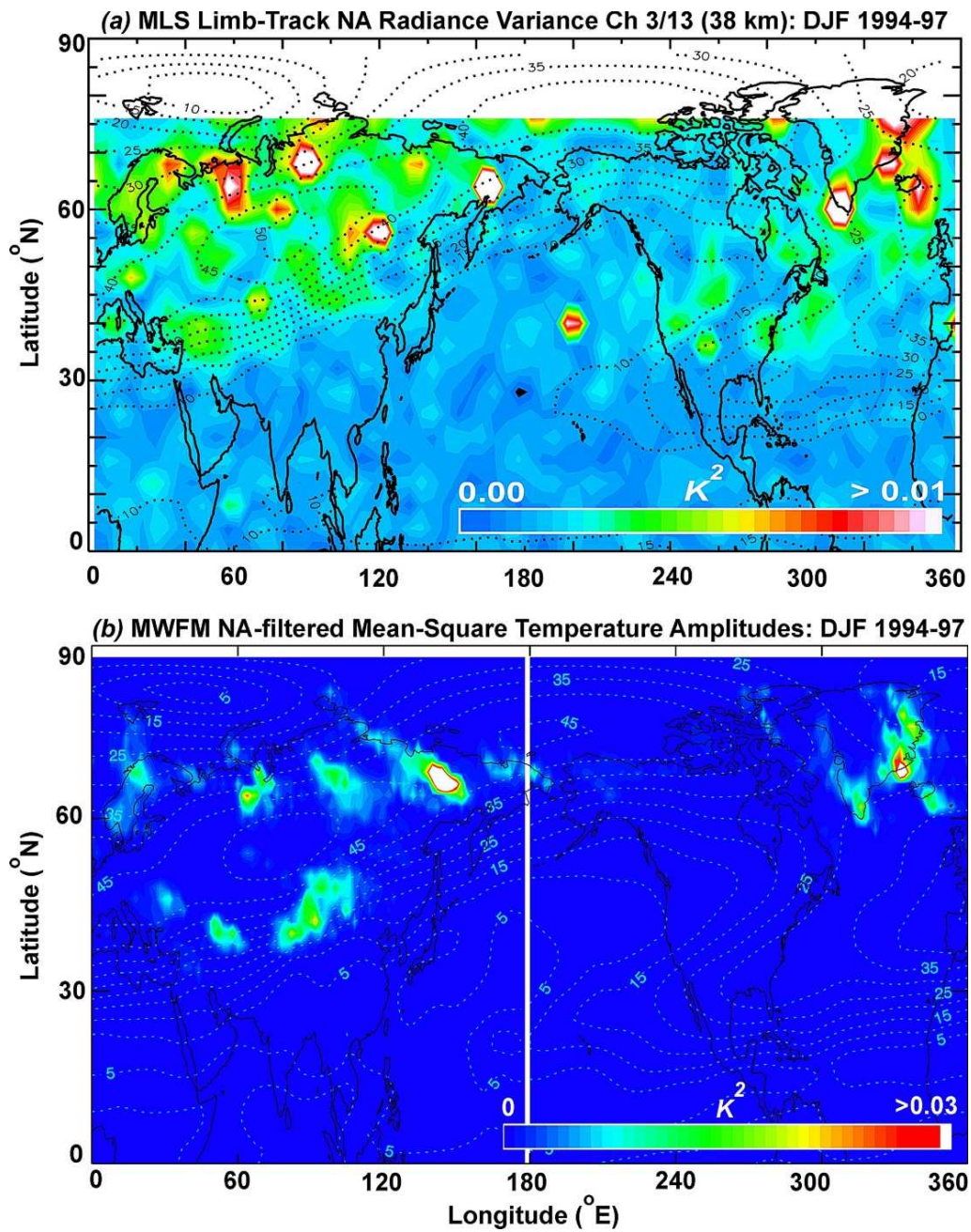


Figure 16: as for Figure 14, but for north-ascending (NA) MLS views.

Figure 16